Magnetic field properties inside the jet of Mrk 421. Multiwavelength polarimetry, including the Imaging X-ray Polarimetry Explorer

Dawoon E. Kim, Laura Di Gesu, Ioannis Liodakis, Alan P. Marscher, Svetlana G. Jorstad, Riccardo Middei, Herman L. Marshall, Luigi Pacciani, Iván Agudo, Fabrizio Tavecchio, et al.

To cite this version:

Dawoon E. Kim, Laura Di Gesu, Ioannis Liodakis, Alan P. Marscher, Svetlana G. Jorstad, et al.. Magnetic field properties inside the jet of Mrk 421. Multiwavelength polarimetry, including the Imaging X-ray Polarimetry Explorer. Astronomy and Astrophysics - A&A, 2024, 681, 10.1051/0004-6361/202347408 . insu-04414249

HAL Id: insu-04414249
https://insu.hal.science/insu-04414249v1

Submitted on 24 Jan 2024

A&A 681, A12 (2024)
https://doi.org/10.1051/0004-6361/202347408

Astronomy & Astrophysics

Magnetic field properties inside the jet of Mrk 421

Multiwavelength polarimetry, including the Imaging X-ray Polarimetry Explorer

Dawoon E. Kim[1,2,3], Laura Di Gesu[4], Ioannis Liodakis[5], Alan P. Marscher[6], Svetlana G. Jorstad[6,7], Riccardo Middei[8,9], Herman L. Marshall[10], Luigi Pacciani[1], Iván Agudo[11], Fabrizio Tavecchio[12], Nicoló Cibrario[13,14], Stefano Tugliani[13], Raffaella Bonino[14,13], Michela Negro[15,16,17], Simonetta Puccetti[8], Francesco Tombesi[3,18,19], Enrico Costa[1], Immacolata Donnarumma[4], Paolo Soffitta[1], Tsunefumi Mizuno[20], Yasushi Fukazawa[21,20,22], Koji S. Kawabata[21,20,22], Tatsuya Nakaoka[20], Makoto Uemura[21,20,22], Ryo Imazawa[21], Mahito Sasada[23], Hiroshi Akitaya[24], Francisco Josè Aceituno[11], Giacomo Bonnoli[12,11], Vìctor Casanova[11], Ioannis Myserlis[25,26], Albrecht Sievers[25], Emmanouil Angelakis[27], Alexander Kraus[26], Whee Yeon Cheong[28,29], Hyeon-Woo Jeong[28,29], Sincheol Kang[28], Sang-Hyun Kim[28,29], Sang-Sung Lee[28,29], Beatriz Agìs-Gonzàlez[11], Alfredo Sota[11], Juan Escudero[11], Mark Gurwell[30], Garrett K. Keating[30], Ramprasad Rao[30], Pouya M. Kouch[5,31], Elina Lindfors[5], Ioakeim G. Bourbah[32], Sebastian Kiehlmann[33,32], Evangelos Kontopodis[32], Nikos Mandarakas[33,32], Stylianos Romanopoulos[33,32], Raphael Skalidis[34,33,32], Anna Vervelaki[32], Sergey S. Savchenko[7,35,36], Lucio A. Antonelli[9,8], Matteo Bachetti[37], Luca Baldini[38,39], Wayne H. Baumgartner[40], Ronaldo Bellazzini[38], Stefano Bianchi[41], Stephen D. Bongiorno[40], Alessandro Brez[38], Niccoló Bucciantini[42,43,44], Fiamma Capitanio[1], Simone Castellano[38], Elisabetta Cavazzuti[4], Chien-Ting Chen[45], Stefano Ciprini[18,8], Alessandra De Rosa[1], Ettore Del Monte[1], Niccoló Di Lalla[46], Alessandro Di Marco[1], Victor Doroshenko[47], Michal Dovčiak[48], Steven R. Ehlert[40], Teruaki Enoto[49], Yuri Evangelista[1], Sergio Fabiani[1], Riccardo Ferrazzoli[1], Javier A. Garcia[50], Shuichi Gunji[51], Kiyoshi Hayashida[52], Jeremy Heyl[53], Wataru Iwakiri[54], Philip Kaaret[40], Vladimir Karas[48], Fabian Kislat[55], Takao Kitaguchi[49], Jeffery J. Kolodziejczak[40], Henric Krawczynski[56], Fabio La Monaca[1], Luca Latronico[14], Simone Maldera[14], Alberto Manfreda[38], Frédéric Marin[57], Andrea Marinucci[4], Francesco Massaro[14,13], Giorgio Matt[41], Ikuyuki Mitsuishi[58], Fabio Muleri[1], C.-Y. Ng[59], Stephen L. O'Dell[40], Nicola Omodei[46], Chiara Oppedisano[14], Alessandro Papitto[9], George G. Pavlov[60], Abel L. Peirson[46], Matteo Perri[8,9], Melissa Pesce-Rollins[38], Pierre-Olivier Petrucci[61], Maura Pilia[37], Andrea Possenti[37], Juri Poutanen[31], Brian D. Ramsey[40], John Rankin[1], Ajay Ratheesh[1], Oliver Roberts[45], Roger W. Romani[46], Carmelo Sgró[38], Patrick Slane[30], Gloria Spandre[38], Doug Swartz[45], Toru Tamagawa[49], Roberto Taverna[62], Yuzuru Tawara[58], Allyn F. Tennant[40], Nicholas E. Thomas[40], Alessio Trois[37], Sergey S. Tsygankov[31], Roberto Turolla[62,63], Jacco Vink[64], Martin C. Weisskopf[40], Kinwah Wu[63], Fei Xie[65,1], and Silvia Zane[63]

(Affiliations can be found after the references)

Received 9 July 2023 / Accepted 6 October 2023

ABSTRACT

Aims. We aim to probe the magnetic field geometry and particle acceleration mechanism in the relativistic jets of supermassive black holes.
Methods. We conducted a polarimetry campaign from radio to X-ray wavelengths of the high-synchrotron-peak (HSP) blazar Mrk 421, including Imaging X-ray Polarimetry Explorer (IXPE) measurements from 2022 December 6–8. During the IXPE observation, we also monitored Mrk 421 using *Swift*-XRT and obtained a single observation with *XMM-Newton* to improve the X-ray spectral analysis. The time-averaged X-ray polarization was determined consistently using the event-by-event Stokes parameter analysis, spectropolarimetric fit, and maximum likelihood methods. We examined the polarization variability over both time and energy, the former via analysis of IXPE data obtained over a time span of 7 months.
Results. We detected X-ray polarization of Mrk 421 with a degree of $\Pi_X = 14 \pm 1\%$ and an electric-vector position angle $\psi_X = 107 \pm 3°$ in the 2–8 keV band. From the time variability analysis, we find a significant episodic variation in ψ_X. During the 7 months from the first IXPE pointing of Mrk 421 in 2022 May, ψ_X varied in the range 0° to 180°, while Π_X remained relatively constant within ~10–15%. Furthermore, a swing in ψ_X in 2022 June was accompanied by simultaneous spectral variations. The results of the multiwavelength polarimetry show that Π_X was generally ~2–3 times greater than Π at longer wavelengths, while ψ fluctuated. Additionally, based on radio, infrared, and optical polarimetry, we find that the rotation of ψ occurred in the opposite direction with respect to the rotation of ψ_X and over longer timescales at similar epochs.
Conclusions. The polarization behavior observed across multiple wavelengths is consistent with previous IXPE findings for HSP blazars. This result favors the energy-stratified shock model developed to explain variable emission in relativistic jets. We considered two versions of the model, one with linear and the other with radial stratification geometry, to explain the rotation of ψ_X. The accompanying spectral variation during the ψ_X rotation can be explained by a fluctuation in the physical conditions, for example in the energy distribution of relativistic electrons. The opposite rotation direction of ψ between the X-ray and longer wavelength polarization accentuates the conclusion that the X-ray emitting region is spatially separated from that at longer wavelengths. Moreover, we identify a highly polarized knot of radio emission moving down the parsec-scale jet during the episode of ψ_X rotation, although it is unclear whether there is any connection between the two events.

Key words. BL Lacertae objects: individual: HSP – galaxies: jets – polarization – relativistic processes – magnetic fields

1. Introduction

Relativistic jets from active galactic nuclei (AGNs) are the most luminous long-lived phenomena across the entire electromagnetic spectrum in the universe. This characteristic of jets makes them natural laboratories that can be studied through multiwavelength and multi-messenger observations from radio to γ-rays.

Blazars are a subclass of AGN in which a relativistic plasma jet, propelled from the vicinity of a supermassive black hole, is aligned closely with our line of sight (e.g., Hovatta & Lindfors 2019). The emission from the jet is relativistically boosted toward us and therefore dominates the spectral energy distribution (SED). The SED typically displays two broad nonthermal radiation components. The lower-frequency component is generally ascribed to be synchrotron emission from relativistic electrons. On the other hand, interpretations of the higher-frequency component fall into two different scenarios: leptonic and hadronic models. In the case of the leptonic model, the high-energy emission is attributed to Compton scattering of synchrotron photons (synchrotron self-Comptonization; e.g., Jones et al. 1974; Maraschi et al. 1992) or photons from outside the jet (e.g., Dermer & Schlickeiser 1993; Sikora et al. 1994). The hadronic scenario explains the high-energy emission as proton synchrotron radiation (e.g., Aharonian 2000; Böttcher et al. 2013) or photo-pion production (e.g., Mannheim 1993).

Blazars are subclassified into three different types, depending on the frequency of the synchrotron peak of the SED. Low-synchrotron-peak blazars have a peak frequency below 10^{14} Hz, intermediate-synchrotron-peak blazars between 10^{14} Hz and 10^{15} Hz, and high-synchrotron-peak (HSP) blazars above 10^{15} Hz (Abdo et al. 2010). Thus, among these subclasses, HSP blazars feature a synchrotron spectrum that smoothly connects from radio to X-ray bands (Fossati et al. 1998). Studies of HSP blazars therefore provide an opportunity to probe the geometry and dynamics of the magnetic field components present in the synchrotron emission features of the jet.

In this respect, multiwavelength polarimetry can be a prominent diagnostic tool for investigating the particle acceleration processes and the geometrical characteristics of the magnetic field inside the jet (e.g., Rybicki & Lightman 1979; Zhang 2019; Böttcher 2019; Tavecchio 2021). Until recently, polarimetric observations of blazars had been limited to optical and radio bands. However, the successful launch of the Imaging X-ray Polarimetry Explorer (IXPE) in late 2021 (Weisskopf et al. 2022) has extended multiwavelength polarimetry up to the X-ray energy band. IXPE is a joint mission of NASA and the Italian Space Agency (Agenzia Spaziale Italiana, ASI). It carries three identical X-ray telescope systems, called detector units (DUs), that correspond to three gas pixel detectors (GPDs; Costa et al. 2001) and three mirror module assemblies. IXPE measures linear polarization in the 2–8 keV band from the photoelectric track produced by the interaction of X-ray photons and gas inside each GPD.

Mrk 421 (redshift, $z = 0.030$) is the brightest HSP blazar at X-ray energies and therefore a prime target for measuring polarization with IXPE (Liodakis et al. 2019). Indeed, IXPE securely detected linear polarization at a level exceeding 10% during a two-day pointing of Mrk 421 in May 2022 (Di Gesu et al. 2022). In addition, during subsequent observations in June 2022, smooth rotation of the electric-vector position angle, ψ_X, was discovered (Di Gesu et al. 2023), in contrast to the relatively stable polarization degree and direction found for a few other HSP blazars (e.g., Liodakis et al. 2022; Middei et al. 2023). This finding can be interpreted as evidence for a helical magnetic field inside the X-ray emitting portion of the jet. Furthermore, if the X-ray emission, and therefore helical field, occurs mainly in the innermost jet, then such rotations of ψ_X should be routinely observed. If so, X-ray observations can probe the section of the jet where the flow is accelerated and collimated (Marscher et al. 2008, 2010).

Here we report the results of a new IXPE observation of Mrk 421, conducted as part of a multiwavelength campaign. In Sect. 2 we present the analysis of the time-averaged data and search for variability in the polarization properties as a function of time and photon energy. To do this, we compared our findings with the results of the previous three IXPE observations and investigated the polarization variability on long timescales. Next, in Sect. 3, we report the multiwavelength polarimetry results obtained from simultaneous and quasi-simultaneous measurements. Based on these results, we propose possible geometrical and physical interpretations of the magnetic field geometry inside the jet of Mrk 421 in Sect. 4. Finally, we summarize our conclusions in Sect. 5.

2. X-ray polarization of Mrk 421

Previously, IXPE observed Mrk 421 three times: 2022 May 4-6 (hereafter Obs. 1), 2022 June 4–6 (Obs. 2), and 2022 June 7–9 (Obs. 3) (Di Gesu et al. 2022, 2023). Here we focus on an additional observation (Obs. ID: 02004401, Obs. 4) conducted from UTC 15:30 on 2022 December 6 to 04:00 on December 8, with a ~ 74 ks net exposure time. During the IXPE pointing, Mrk 421 was in a normal X-ray activity state (e.g., Liodakis et al. 2019), with a 2–8 keV flux of $\sim 2 \times 10^{-10}$ erg s^{-1} cm^{-2}. From this observation, we derived the time-averaged polarization degree Π_X and electric-vector position angle ψ_X over the entire exposure. In order to investigate the X-ray polarization variability, we also performed time- and energy-resolved analysis.

We also observed Mrk 421 with X-Ray Multi-Mirror Mission (hereafter *XMM-Newton*) EPIC-pn camera on 2022 December 7 for 7.5 ks. In addition, the *Neil Gehrels Swift* Observatory (hereafter *Swift*-XRT) monitored the blazar to improve the spectral and temporal coverage. Table 1 presents a summary of the X-ray observations. Detailed information on the data reduction procedures is presented in Appendix A. Throughout the manuscript, errors are given at the standard 1σ (68%) confidence level.

2.1. Time-averaged polarization properties

We derived the linear polarization parameters from Obs. 4 using four different methods: (1) the Kislat et al. (2015) method that is implemented in the `PCUBE` algorithm in `ixpeobssim` (Baldini et al. 2022), (2) an event-based maximum likelihood (ML) method Marshall (2021b) that includes simultaneous background estimation, (3) the spectropolarimetric analysis described in Strohmayer (2017) using `XSPEC`, and (4) a maximum likelihood spectropolarimetric (MLS) fit implemented by the multi nest algorithm. Table 1 summarizes the Π_X and ψ_X values obtained from these methods.

First, using the Kislat et al. (2015) method, we estimated $\Pi_X = 13 \pm 2\%$ and $\psi_X = 107 \pm 3°$ in the 2–8 keV band after background subtraction from the three combined DUs. The `PCUBE` measurement includes the spectral-model-independent polarization properties over a given energy and time range (Kislat et al. 2015). We derived Π_X and ψ_X from the normalized Stokes parameters Q ($\mathcal{Q} \equiv Q/I$) and U ($\mathcal{U} \equiv U/I$), according to $\Pi_X = \sqrt{(\mathcal{Q})^2 + (\mathcal{U})^2}$ and $\psi_X = 1/2 \tan^{-1}(\mathcal{U}/\mathcal{Q})$. Error estimation was calculated based on Kislat et al. (2015) and Muleri (2022). Figure 1 indicates the detection significance of this measurement in the form of a polarization contour plot.

The second method uses an event-based ML method to determine Q and U (Marshall 2021b). The method accounts for background using data from an annulus about the target by including a term in the likelihood, as used in the analysis of the IXPE data of Cen A (Ehlert et al. 2022). Source events were selected from a region of 60″ radius about the source centroid, while the background events were selected from an annulus with inner and outer radii of 200″ and 300″. In this case, $\Pi_X = 13 \pm 1\%$ and $\psi_X = 107 \pm 3°$.

Next, the spectropolarimetric analysis examined the X-ray spectra and polarization properties based on spectral modeling with `XSPEC` (version 12.13.0c; Arnaud et al. 1996). With this

Table 1. Results of the X-ray polarimetric and spectral observations of Mrk 421.

Telescope (Method [(1)])	Band	Dates	X-ray polarization		X-ray flux [(2)]
	(keV)	(YYYY-MM-DD)	Π_X(%)	ψ_X (°)	(10^{-10} erg s^{-1} cm^{-2})
IXPE Obs. 4 (`PCUBE`)	2.0–8.0	2022-12-06–08	13 ± 2	107 ± 3	–
IXPE Obs. 4 (`ML`)	2.0–8.0	2022-12-06–08	13 ± 1	107 ± 3	–
IXPE Obs. 4 (`XSPEC`)	2.0–8.0	2022-12-06–08	14 ± 1	107 ± 3	2.25 ± 0.04
IXPE Obs. 4 (`MLS`)	2.0–8.0	2022-12-06–08	13 ± 1	109 ± 3	–
Swift-XRT	0.3–10.0	2022-12-06	–	–	3.20 ± 0.06
XMM-Newton	0.3–10.0	2022-12-07	–	–	2.04 ± 0.04
Swift-XRT	0.3–10.0	2022-12-08	–	–	2.47 ± 0.05
IXPE Obs. 3 (`PCUBE`)	2.0–8.0	2022-06-07–09	10 ± 1	Rotation	3.02 ± 0.02
IXPE Obs. 2 (`PCUBE`)	2.0–8.0	2022-06-04–06	10 ± 1	Rotation	1.57 ± 0.01
IXPE Obs. 1 (`PCUBE`)	2.0–8.0	2022-05-04–06	15 ± 2	35 ± 4	0.87 ± 0.003

Notes. [(1)]Methods are described in Sect. 2.1. [(2)]X-ray flux in the 2–8 keV band.

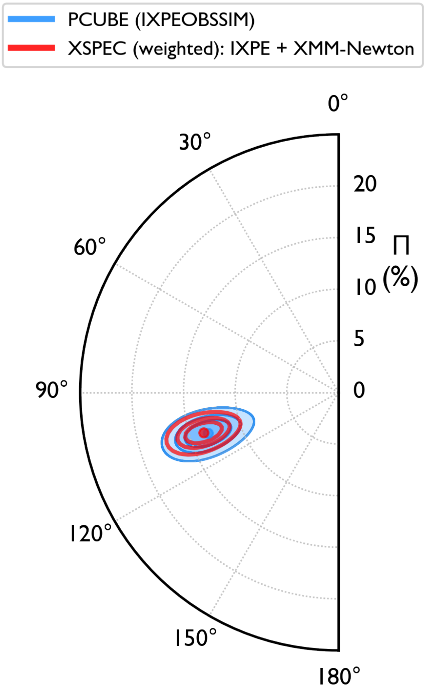

Fig. 1. Polarization contours from Obs. 4. Contours represent the significance of the time-averaged polarization detected with confidence levels of 68.27%, 90.00%, and 99.00%, with two degrees of freedom. The blue contour indicates the values of Π_X and ψ_X derived via the `PCUBE` methods, and the red contours show the same properties from simultaneous IXPE and *XMM-Newton* spectropolarimetric analysis. The radial and angular values represent Π_X and ψ_X, respectively, with the latter measured from north through east.

method, we obtained $\Pi_X = 14 \pm 1\%$ and $\psi_X = 107 \pm 3°$. The detection significance of this measurement was $\gtrsim 11\sigma$. The flux was estimated as 2.25 (±0.04) × 10^{-10} erg s^{-1} cm^{-2} over 2–8 keV, the same band over which the IXPE I, Q, and U spectra were obtained. In this analysis, we additionally included the simultaneous *XMM-Newton* data in order to refine the constraints on the spectral shape over the 0.3–10 keV energy range. The cross-calibration factors among all the spectra are accounted for using the `CONSTANT` model, normalized to the *XMM-Newton* spectrum while the other spectra were varied. In all the fits, we considered the Galactic absorption along the line of sight of Mrk 421. For this, we used the `TBABS` model with weighted average column density values from HI4PI Collaboration (2016) ($N_H = 1.34 \times 10^{20}$cm^{-2}). The `WILM` model was applied to take into account metal abundance (Wilms et al. 2000). For the spectral modeling, we first applied a simple power law model (`POWERLAW` in `XSPEC`) to reproduce the I synchrotron spectrum, but the best-fit result was poor, with χ^2/d.o.f. = 3308/651. Hence, we employed the log-parabolic model (`LOGPAR`), in which the photon index varies with energy following a log parabola function Massaro et al. 2004:

$$N(E) = K(E/E_{\rm pivot})^{(\alpha - \beta \log(E/E_{\rm pivot}))}, \tag{1}$$

where the pivot energy $E_{\rm pivot}$ is a scaling factor, α describes the slope of the photon spectrum at $E_{\rm pivot}$, β expresses the spectral curvature, and K denotes a normalization constant. This spectral model generally describes a typical HSP blazar spectrum well, including that of Mrk 421, both in quiescence and in flaring states (Donnarumma et al. 2009; Baloković et al. 2016). As the photon index varies with energy in this model, the choice of reference energy $E_{\rm pivot}$ changes the determined value of α. In our spectral fit, we fixed the pivot energy to 5.0 keV (e.g., Baloković et al. 2016; Middei et al. 2022). In this case, the α parameter approximately corresponds to the photon index over 3.0–7.0 keV. In our spectral fitting, we also allowed the values of α, β, and K to vary. These free parameters are coupled with the reference spectrum, which here is the *XMM-Newton I* spectrum over the same 2–8 keV band to which the three IXPE DUs are sensitive. Finally, the X-ray polarimetric measurements were constrained by the `POLCONST` model based on the Stokes parameter fits. Consequently, we obtained statistically acceptable fits, with χ^2/d.o.f. = 740/650, above 99% confidence level. Figure A.1 and Table A.1 present the parameter values of our best-fit results. We note that in the Stokes-spectra-decoupled case, which only fits I spectra without involving `POLCONST`, the best-fit results obtained the same values as we derived from the simultaneous spectropolarimetric fit.

Finally, the MLS method was also applied to determine the polarization properties for the `POWERLAW` spectral model. With this procedure, we derived the polarization and spectral properties to be $\Pi_X = 13 \pm 1\%$ and $\psi_X = 109 \pm 3°$.

Therefore, the X-ray polarization properties we derived using four different methods are consistent within the uncertainties (see Table 1). The small differences can be explained by the fact that the `PCUBE` analysis estimated spectral-model-independent polarization properties, while the `XSPEC` methods

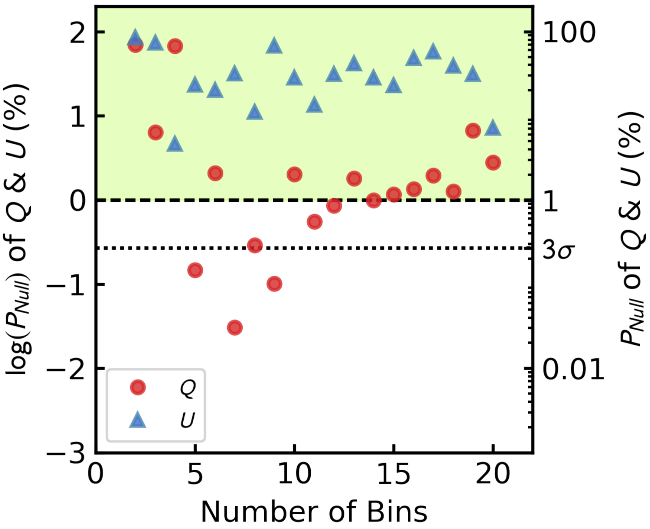

Fig. 2. Null-hypothesis probability of the χ^2 test for time variability of the $\mathcal{Q}$ (red) and $\mathcal{U}$ (blue) Stokes parameters with the constant model for different numbers of time bins for Obs. 4. The left and right vertical axes correspond to the probability values in logarithmic and linear scales, respectively. The green shaded area indicates that the null-hypothesis probability is above the 1% significance level. The dashed and dotted black lines located in the middle of the panel represent 1% and 3σ (99.73%) probability, respectively.

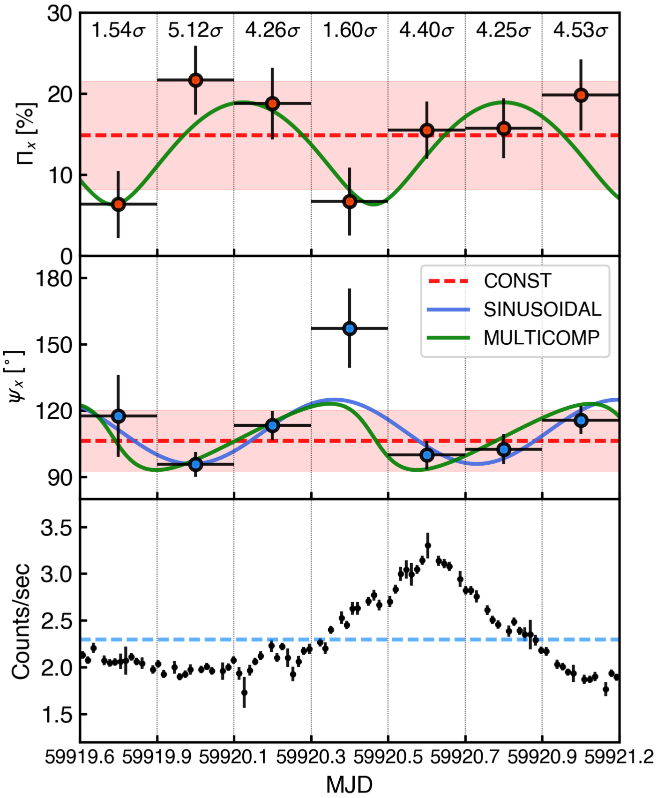

Fig. 3. IXPE polarization and photon counts versus time during Obs. 4. From top to bottom: Π_X, ψ_X, and count rates. Polarization results are from a time-resolved analysis with seven identical 19 ks time bins. The detection significance for each bin is displayed at the top of the figure. In the Π_X and ψ_X panels, dashed red lines denote a fit to a constant function; the shaded area corresponds to $\leq 3\sigma$ uncertainty. In addition, the solid blue and green lines indicate the best-fit result with the sinusoidal and multicomponent model, respectively. The dashed blue line in the light curve indicates the average value during the observation.

take into account the best fit from the spectral modeling. Furthermore, among the current choices, only the `XSPEC` method can improve sensitivity by applying event weight methods introduced by Di Marco et al. (2022). Overall, we find that the Π_X and ψ_X results are robust, with modest statistical errors (see Fig. 1).

2.2. Polarization variability

We investigated whether the polarization varies as a function of time or energy. We tested the time dependence using two methods. In the first one, we determined the null-hypothesis probability with the χ^2 test using the combined `PCUBE` and `XSPEC` analysis (e.g., Di Gesu et al. 2022, 2023; Gianolli et al. 2023). For the second method, we used the unbinned event-based ML analysis implemented in Marshall (2021a). With this method, we can avoid the error that can be caused by subjective selection bias resulting from the binning criteria.

The first method measured each normalized Stokes parameter value by dividing the data into identical time spans that depended on the selected number of bins (e.g., 2 bins = 100 ks/2 bins = 50 ks/bin). In particular, we split Obs. 4 into 2–20 time bins. We then compared $\mathcal{Q}$ and $\mathcal{U}$, which followed a Gaussian error distribution, with the results from fitting each parameter treated as constant over time (i.e., $\mathcal{Q}(t) = \mathcal{Q}_0$ and $\mathcal{U}(t) = \mathcal{U}_0$). The result of fitting the constant model was calibrated for each number of bins. We then calculated the χ^2 and the null-hypothesis probability (for the corresponding degrees of freedom) for each case. Figure 2 indicates the null-hypothesis probability as a function of the number of bins. In this figure, the green-shaded area ($P_{\rm Null} > 1\%$) corresponds to cases where the data are statistically consistent with values of $\mathcal{Q}$ and $\mathcal{U}$ that are constant in time. Conversely, if the points lie outside the region ($P_{\rm Null} < 1\%$), it implies that the polarization varies with time. As seen in Fig. 2, we found that splitting the $\mathcal{Q}(t)$ light curves with 5, 7, 8, 9, 11, 12, and 14 time bins does not produce a good fit with the constant model ($P_{\rm Null} < 1\%$). The case of 7 time bins has the smallest null-hypothesis probability, with χ^2/d.o.f. = 25.26/6, beyond the 3σ confidence level. In the polarization light curve of Obs. 4 with seven identical time bins (Fig. 3), we can see that ψ_X varies from the second to the fourth bin, after which it returns to a more stable value near that of the first three bins. We estimate the rotation rate of this variation as $\dot{\psi} \sim 92$ °/day (change by 61° over ~57 ks from the second to the fourth bin). This result is comparable to the rotation rate of $\dot{\psi} = 85°$/day reported in Di Gesu et al. (2023).

Additionally, in order to examine the possibility of continuous change of ψ_X, we tested whether a sinusoidal function ($\psi_X(t) = A\sin(Ct - D) + B$) provides a better fit of $\psi_X(t)$ with respect to a constant function corresponding to the mean value of ψ_X over 7 time bins (blue line in Fig. 3). This approach yielded a smaller χ^2/d.o.f. value of 4.75/3, with a Bayesian information criterion (BIC) of 12.53, than the constant model (χ^2/d.o.f. = 16.66/6, BIC = 18.60).

As a second approach, we employed a ML method that allows for ψ_X rotation in each interval, as described elsewhere (Di Gesu et al. 2023) and shown in Fig. 4. Briefly, the ML method is used (see Sect. 2.1) for eight equal time intervals but also allowing for ψ_X rotation during the time interval, as an "uninteresting" parameter. This approach prevents ψ_X rotations during a time interval from reducing the average

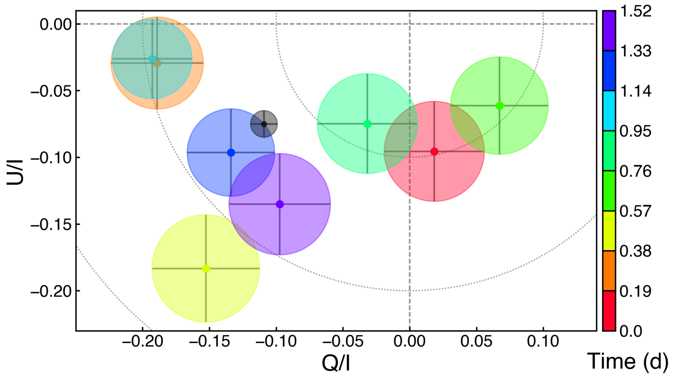

Fig. 4. Time variability of the Q and $\mathcal{U}$ Stokes parameters during Obs. 4. Each circle indicates the 1σ uncertainties of eight identical time intervals, derived using an event-based ML technique as described in Di Gesu et al. (2023). The black circle shows the time-averaged polarization. Each color represents a time interval from the start to the end of Obs. 4.

polarization of that interval, which is important when there are large ψ_X changes. For example, Fig. 4 shows that there appear to be large, nearly 90° ψ_X shifts between intervals one and two and between intervals three and four. As a result, we confirmed that ψ_X varied over time during Obs. 4 with ~4.5σ confidence.

In addition, with a ML method, we tested a more complex model fit – the multicomponent model (Pacciani et al., in prep.), which involves the convolution of constant and rotating polarization components – to check the possibility of continuous variation within the Obs. 4 period. The details of this model are described in Appendix B. From this test, we computed the significance of the multicomponent model relative to the constant polarization model based on the delta likelihood, $\Delta S' = S'(\Pi_0, \Psi_0, 0) - S'(\Pi_1, \Psi_1, \Pi_2, \Psi_2, \omega)$. We obtained a decrease in the likelihood estimator, $\Delta L = -32.4$, which follows a chi-square distribution with three degrees of freedom. Hence, the constant polarization model is rejected in favor of the multicomponent model, at the ~5σ confidence level that this result occurred by chance. The parameters estimated with the multicomponent model are reported in Table 2. The observed discrepancy between the rotation rate measured from the multicomponent model (i.e., $\omega = 245\,°/\text{day}$) and the rate estimated directly from the light curve (i.e., $\dot{\psi} \sim 92°/\text{day}$) can be explained by differences in physical interpretation. The multicomponent model assumes a persistent presence of the rotating component in conjunction with the constant emission component, while the other case assumes that the emission originates from a single dominant component. The multicomponent model is indicated with a green line in Fig. 3.

Therefore, based on these different methods, we conclude that we have found an episodic ψ_X variation over time during Obs. 4. Furthermore, the results of sinusoidal and multicomponent models suggest that the variations may be attributed to continuous changes in stable components. However, due to differences in the analysis methods employed, these two models were not compared in this study. Moreover, since these model fit results were derived as relative outcomes compared to the constant model, we cannot rule out the possibility of encountering more complex components and potential stochastic variations.

We also tested whether the X-ray polarization depends on energy by applying the same null-hypothesis probability test discussed above, but with the IXPE energy band (2–8 keV) divided into smaller ranges. We did so for two energy bins (2–4 and 4–8 keV), as well as three energy bins (2–4, 4–6, and 6–8 keV), up to 12 energy bins. We find no statistically significant differences with a constant fit, as $P_{\text{Null}} \geq 13\%$ from both Q and $\mathcal{U}$; hence, the data are consistent with energy-independent X-ray polarization.

Table 2. Parameters for the multicomponent model.

$R_1 \cdot \Pi_1$ (%)	Ψ_1 (°)	$(1 - R_1) \cdot \Pi_2$ (%)	Ψ_2^0 (°)	ω (°/day)
12.6 ± 1.6	108 ± 4	6.3 ± 1.8	−96 ± 17	246 ± 23

2.3. X-ray polarization and spectral variability across multiple IXPE observations

Significant X-ray polarization from Mrk 421 has been detected at four epochs with IXPE (see Table 1). Figure 5 shows error contours for both time-averaged and time-resolved data of each observation. Over the seven months from IXPE Obs. 1 to Obs. 4, the value of ψ_X varied widely, with a continuous rotation over 180° observed during Obs. 2 and Obs. 3. In contrast, measurements of Π_X for all events were similar within a range of 10-15%, even though the time-averaged Π_X of Obs. 2 and Obs. 3 appears to be clearly lower than in the other cases due to dilution by the changing of ψ_X. However, the mean value of Π_X during periods of non-rotation of ψ_X (Obs. 1 and Obs. 4) was 14 ± 2%, a factor of 1.4 ± 0.2 higher than the value of 10 ± 1% during the rotation (Obs. 2 and Obs. 3). This result is similar to the findings of previous optical polarimetry studies: (1) Blinov et al. (2016b) observed that the ratio of Π_O of rotating to that of nonrotating cases is less than 1 in 18 out of the 27 observed rotations, and (2) Jermak et al. (2016) reported a 26% reduction in the average Π_O during rotational periods compared to non-rotational periods. Nonetheless, because of the limited amount of X-ray polarization data, this result should be verified with an increased number of measurements from future X-ray polarimetry monitoring observations.

The radio electric-vector position angle $\psi_{43\,\text{GHz}}$ obtained from the 43 GHz Very Long Baseline Array (VLBA) observations (black line in Fig. 5) differs from ψ_X and which also changes by 70° over the 7 months from Obs. 1 to Obs. 4. The pronounced variation in ψ_X and $\psi_{43\,\text{GHz}}$ contrasts with the steadier X-ray polarization observed in other sources of the same subclass of blazars, whose synchrotron SED peaks at X-ray frequencies (i.e., Mrk 501; Liodakis et al. 2022).

We also investigated the spectral properties and X-ray activity of Mrk 421 through *Swift*-XRT monitoring observations. Figure 6 presents the α and β spectral parameters obtained from the `LOGPAR` model fit. We also derived the X-ray flux in the soft (0.3–2 keV), F_{soft}, and hard (2–10 keV), F_{hard}, energy bands, and define the hardness ratio as $(F_{\text{hard}} - F_{\text{soft}})/(F_{\text{hard}} + F_{\text{soft}})$. We have found that the α parameter, representing the slope of the spectrum at the pivot energy, maintained similar values in Obs. 1 and Obs. 4. However, during Obs. 2 and Obs. 3, α decreased with time. In addition, the hardness ratio also varied during the ψ_X rotation, while its value in Obs. 1 was consistent with that in Obs. 4. Nonetheless, in the case of Obs. 4, *Swift*-XRT observations were conducted only at the beginning and shortly after the IXPE pointing; thus, we cannot exclude the possibility of variations in spectral properties during Obs. 4.

The X-ray fluxes of Mrk 421 during all epochs of IXPE observations were within 1σ of the median historical value (e.g.,

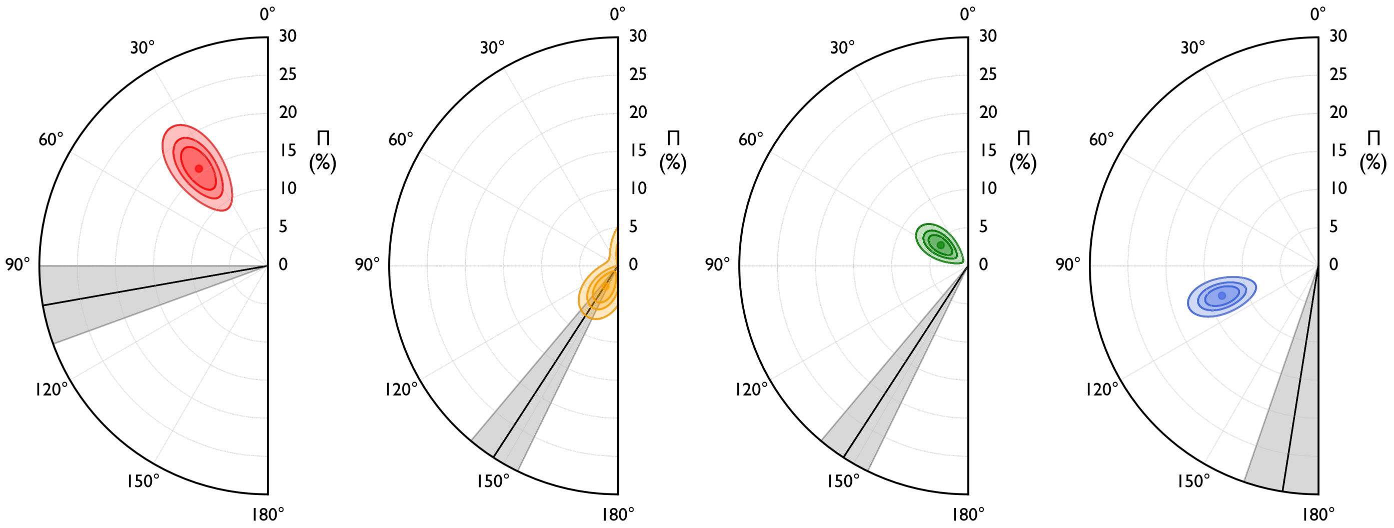

Time-averaged polarization contours.

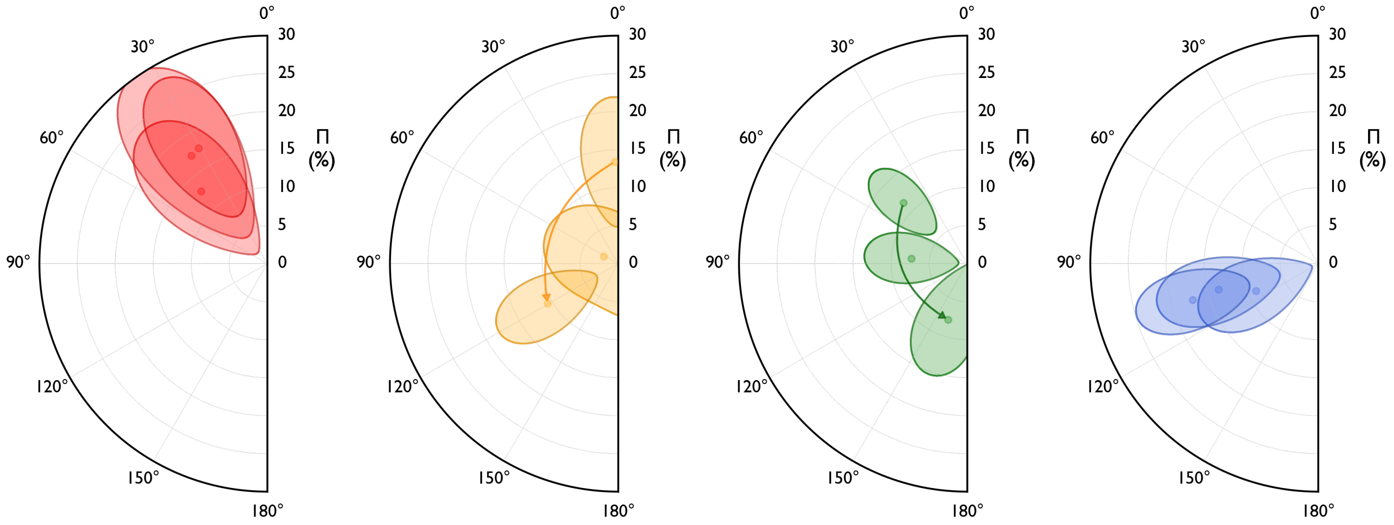

Time-resolved polarization contours.

Fig. 5. Time-averaged and time-resolved polarization contours of four multiple IXPE observations. In the top panel, each colored contour represents the significance of the time-averaged polarization detection for the corresponding observation (Obs. 1 in red, Obs. 2 in orange, Obs. 3 in green, and Obs. 4 in blue). Contours are shown at confidence levels of 68.27%, 90.00%, and 99.00%, as determined from a χ^2 test with two degrees of freedom. Additionally, the black line and gray shaded areas indicate the jet's electric-vector position angle in degrees as observed by the VLBA at 43 GHz (Obs. 1 is $100 \pm 10^\circ$, Obs. 2 is $147 \pm 7^\circ$, Obs. 3 is $147 \pm 7^\circ$, and Obs. 4 is $171 \pm 10^\circ$). In the bottom panel, the 99.00% confidence level contours show the time variation in polarization properties as determined by dividing the data into three identical time intervals for each observation. In the cases of Obs. 2 (orange) and Obs. 3 (green), arrows indicate a rotation of ψ_X from the start to the end of the observation.

Liodakis et al. 2019). Nonetheless, we found significant fluctuations during Obs. 2 and Obs. 3. Although the flux variations occurred during all of the IXPE epochs (see, e.g., Fig. 3), the discrepancy between the minimum and maximum counting rates was larger in Obs. 2 and Obs. 3. Therefore, we suggest that the smooth ψ_X rotation behavior may accompany more pronounced spectral and flux fluctuations.

3. Multiwavelength polarization analysis

Multiwavelength campaigns for the first three observations of Mrk 421 are reported in Di Gesu et al. (2022, 2023). During Obs. 4, Mrk 421 was observed with the VLBA, the Effelsberg 100-m Radio Telescope, the Korean VLBI Network (KVN), the Submillimeter Array (SMA), the Kanata Telescope, the Perkins Telescope, and the Sierra Nevada Observatory (SNO; T90 telescope). Details of the observations and observatories can be found in Appendix A.3.

We analyzed VLBA data obtained for Mrk 421 within the BEAM-ME (Blazars Entering the Astrophysical Multimessenger Era) program[1] during the period from MJD 59616 (2022 February 5) to MJD 59986 (2023 February 11) to investigate

---

[1] www.bu.edu/blazars/BEAM-ME.html

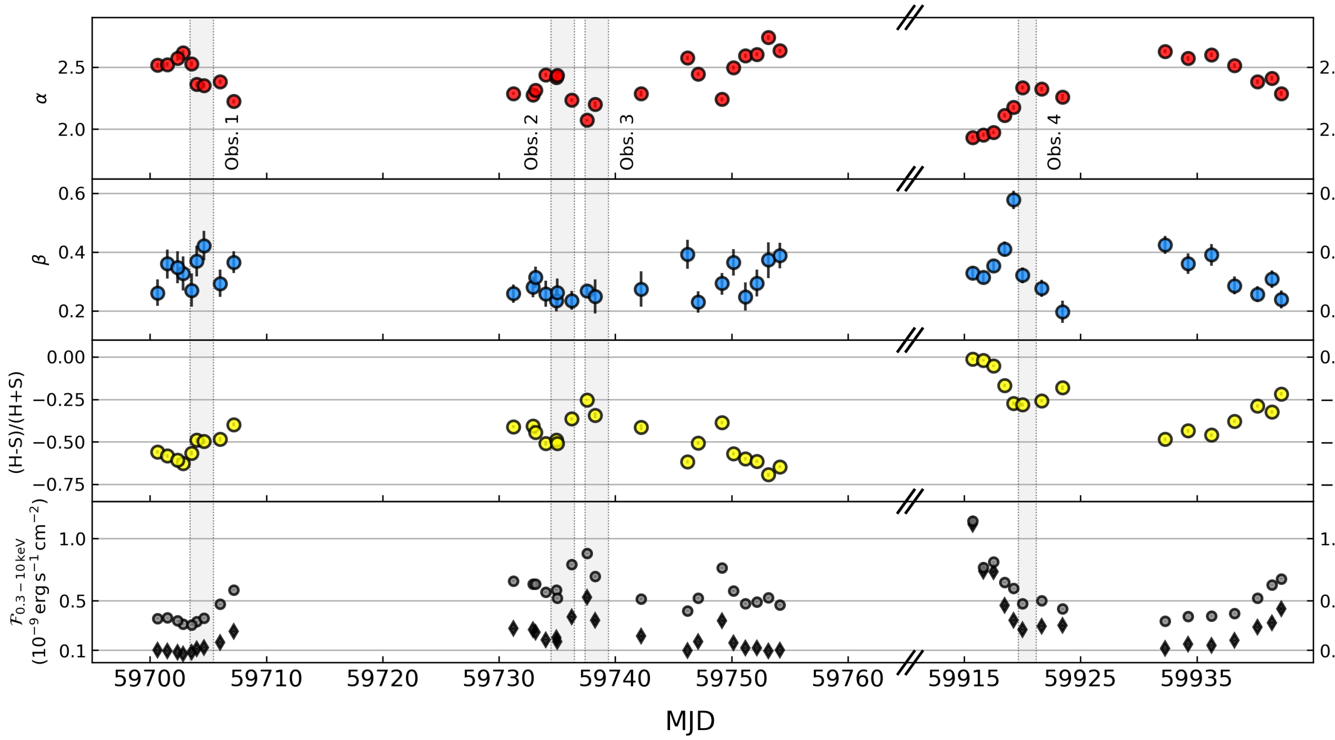

Fig. 6. *Swift*-XRT X-ray spectral parameters and flux versus time of Mrk 421 from a log-parabolic best-fit model with $E_{\mathrm{pivot}} = 5$ keV. From top to bottom: α, β, hardness ratio, and flux in the soft (0.3–2 keV, gray circles) and hard (2–10 keV, black diamonds) energy bands. The time ranges of the IXPE pointings are indicated by the gray shaded regions.

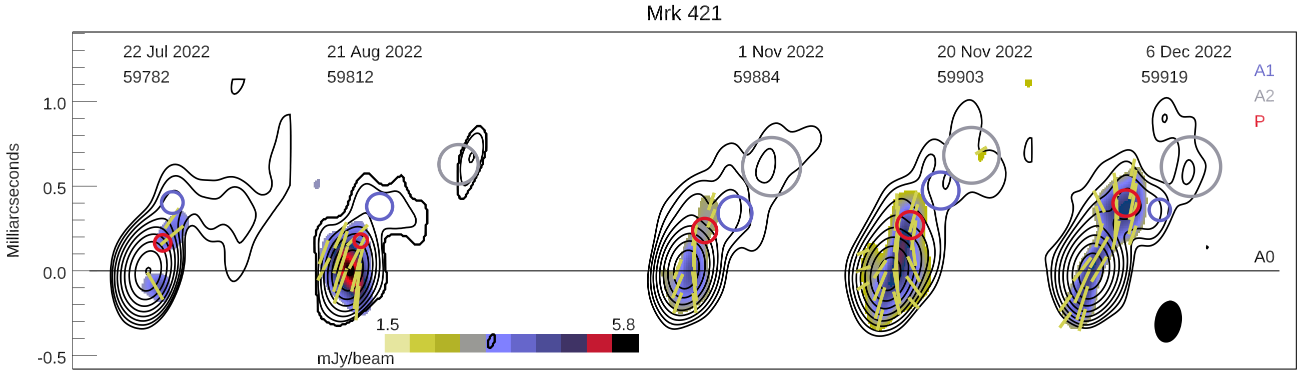

Fig. 7. VLBA total (contours) and polarized (color scale) intensity images of Mrk 421 at 43 GHz. The peak of the total intensity is 295 mJy beam^{-1}. Yellow linear segments within the images indicate the direction of polarization, the black horizontal line marks the position of the core, $A0$, and colored circles indicate locations of jet features $A1$ (blue), $A2$ (gray), and P (red). Images are convolved with the same elliptical Gaussian beam, which is shown in the bottom-right corner by a black ellipse.

the parsec-scale jet behavior during the IXPE observations. The data include total and polarized intensity images at 43 GHz at 12 epochs. The data reduction and modeling are described in Appendix A.4. The parsec-scale jet of Mrk 421 is strongly core-dominated, with the extended jet contributing an average of only 17% of the core flux density at 43 GHz. We consider the core to be a stationary feature of the jet and designate it as $A0$. During the one-year period analyzed here, we have detected two stationary features in the jet in addition to the core, $A1$ and $A2$, located at distances of ~0.4 and ~0.8 mas from $A0$, respectively (see Table A.3). Dominance by stationary structures is a well-documented property of the Mrk 421 jet (Lico et al. 2012; Jorstad et al. 2017; Lister et al. 2021; Weaver et al. 2022). Nonetheless, we have found motion in the jet, which we identify with a prominent polarized feature, P, which has a sub-luminal apparent speed $\beta_{\mathrm{app}} = 0.7 \pm 0.1$ in units of c. Figure 7 presents a sequence of images at epochs where the knot is prominent. Figure A.5 shows that knot P had a high degree of polarization, with ψ_{P} almost aligned with the jet direction, as expected if feature P was a transverse shock in the jet. According to its kinematics, the knot passed through the core on 2022 March 14 (MJD 59653 ± 80; Fig. A.3). If one considers the sizes of $A0$ and P listed in Table A.3, plus the proper motion of P (Appendix A.4), it should have taken 107 ± 19 days for knot P to leave the core completely, which should have occurred within 2022 June 10–July 8. This means that during IXPE Obs. 1, Obs. 2, and Obs. 3, knot P was within the millimeter-wave core.

The Effelsberg 100-m Telescope observation was obtained within the framework of the QUIVER program (Monitoring the Stokes Q, U, I and V Emission of AGN jets in Radio) on 2022 December 2 (MJD 59915.11). The linear polarization was measured at 3 bands: 4.85 GHz, 8.35 GHz and 10.45 GHz. Its polarization degree was found to be $0.9 \pm 0.2\%$, $1.2 \pm 0.4\%$, and $1.2 \pm 0.2\%$. and its polarization angle $96.3 \pm 3.5°$, $134.8 \pm 4.9°$, and $159.2 \pm 7.2°$, respectively. The KVN observations, with the antennas combined to act as a single dish, were performed on 2022 December 9 (MJD 59922.73) at 22, 43, 86, and 129 GHz. The linear polarization was measured as $\Pi_{22\,\mathrm{GHz}} = 2.4 \pm 0.7\%$ along $\psi_{22\,\mathrm{GHz}} = 30 \pm 12°$ at 22 GHz and $\Pi_{43\,\mathrm{GHz}} = 2.7 \pm 0.5\%$ along $\psi_{43\,\mathrm{GHz}} = 142 \pm 9°$ at 43 GHz. The measured values of Π at 86 GHz ($3.1 \pm 2.3\%$) and 129 GHz ($4.4 \pm 2.0\%$) are not significant detections. The polarization was measured with the SMA at 225.5 GHz as $\Pi_{225\,\mathrm{GHz}} = 2.0 \pm 0.3\%$ along position angle $\psi_{225\,\mathrm{GHz}} = 163 \pm 3°$. At the same time, the intrinsic polarization degree (after subtraction of the host-galaxy flux) in the optical R band from SNO was $\Pi_{\mathrm{O}} = 4.6 \pm 1.3\%$ along $\psi_{\mathrm{O}} = 206 \pm 9°$. The Perkins telescope obtained optical R-band polarization covering Obs. 4 from 2022 November 26 (MJD 59909) to December 17 (MJD 59930) to give the average optical polarization parameters just before and after Obs. 4, which can be compared with the SNO measurement. In the infrared J and optical R bands, the Kanata Telescope data (not corrected for the host-galaxy depolarization) yield $\Pi_J = 2.41 \pm 0.02\%$ and $\Pi_{\mathrm{O}} = 2.1 \pm 0.03\%$ along $\psi_J = 176 \pm 0.2°$ and $\psi_{\mathrm{O}} = 167.0 \pm 0.3°$, respectively. The latter is similar to previous Mrk 421 R-band observations with the Kanata Telescope, for which an intrinsic value of $\Pi_{\mathrm{O}} \approx 3.3\%$ was derived (Di Gesu et al. 2023), which is consistent with the SNO measurement. All of the new multiwavelength polarimetry results conducted during Obs. 4 are summarized in Table A.2.

Figure A.2 exhibits the evolution of polarization properties of Mrk 421 obtained from the contemporaneous multiwavelength polarimetry campaign from just before IXPE Obs. 1 to shortly after Obs. 4. Throughout this time period, we find a similar strong chromatic behavior, with 2–3 times higher Π at X-ray rather than at longer wavelengths. In contrast, the infrared, optical, and radio degrees of polarization were similar. Meanwhile, the polarization position angle exhibited marked changes, with different values during the various IXPE pointings. The range of ψ observed in Obs. 1 across millimeter to X-ray wavelengths was ~30°, whereas a larger range of ~90° was evident in Obs. 4. Moreover, Di Gesu et al. (2023) have reported that, during the rotation of ψ_{X} of Obs. 2 and Obs. 3, ψ values at other wavelengths were consistent with each other, with a weak temporal variation. Hence, we conclude that the region where the polarized X-rays are emitted is mostly or completely distinct from that at longer wavelengths.

Furthermore, Mrk 421 exhibited a clockwise ψ_{O} rotation of approximately 120° over ~40 days during the first three IXPE observation periods. Similar behavior has been reported in previous optical polarimetry monitoring studies, where the polarization angle changed by ~180° over ~50 days (Blinov et al. 2015, 2016a, 2018; Jermak et al. 2016; Fraija et al. 2017). The direction of the ψ_{O} rotation was opposite to the counterclockwise ψ_{X} rotation observed by IXPE during Obs. 2 and Obs. 3.

4. Discussion

Previous IXPE observations of the HSP blazars Mrk 421 (Di Gesu et al. 2022, 2023) and Mrk 501 (Liodakis et al. 2022) suggest that an energy-stratified shock can most readily explain the ~2–3 times higher degree of polarization at X-ray rather than at longer wavelengths. In this work, we have found consistent multiwavelength measurements from Obs. 4. In this energy-stratified shock model, the relativistic electrons convert their energy to radiation as they move farther from the shock front (Marscher & Gear 1985; Tavecchio et al. 2018). The particles are efficiently accelerated at the shock front, where the magnetic field is relatively well ordered, and hence emit X-ray synchrotron radiation with relatively high polarization. Conversely, electrons lose energy as they propagate away from the shock, causing them to radiate at longer wavelengths, and the degree of polarization decreases as they encounter increasingly turbulent magnetic fields (Di Gesu et al. 2022, 2023; Liodakis et al. 2022). Hence, higher Π is predicted at higher frequencies. This effect ceases at wavelengths long enough that the electrons radiating at those wavelengths can cross the entire shocked region before losing most of their energy (Marscher & Gear 1985). This limitation can explain the similar polarization from millimeter to optical wavelengths observed in Mrk 421. It is also possible that the longer wavelength emission occurred mainly in a relatively slow sheath surrounding a much faster X-ray emitting spine of the jet (e.g., Di Gesu et al. 2023). This is consistent with the sub-luminal speed we measured for knot P. In this case, the X-ray and longer wavelength polarization properties may not be related, consistent with their different position angles.

We therefore consider two possible geometries for an energy-stratified jet in Mrk 421: linear and radial models, as suggested by Di Gesu et al. (2022, 2023). In the case of linear geometry, the energy stratification and the ψ rotation can be explained by emission features propagating downstream in the jet, following the helical magnetic field. On the other hand, the radial structure can correspond to a helical, rotating innermost region and a surrounding layer, similar to the spine-sheath jet model (Chhotray et al. 2017). The currently available observational data are insufficient to discern between the linear and radial geometries. Nevertheless, the episodic variation in polarization observed during Obs. 4 offers further insights into the internal geometry of the jet. For instance, it implies alternative perspectives on the geometric structure within the jet, including the intricate interactions between coexisting stable and rotating magnetic field structures, as well as stochastic transitions within the dominant magnetic field structure responsible for particle acceleration. Therefore, future observations of polarization variability are expected to yield further evidence about the geometric structure inside the jet.

On the other hand, despite the comparable multiwavelength results reported for Mrk 421 and Mrk 501, we have found a difference in the behavior of ψ_{X} between them. In the case of Mrk 421, $\psi_{43\,\mathrm{GHz}}$ and ψ_{X} exhibited significant variations without any consistent alignment with either each other or the direction of the jet axis. However, in the case of Mrk 501, an alignment was observed (within the uncertainties) between measurements of the position angle of the jet axis, ψ_{X}, and $\psi_{43\,\mathrm{GHz}}$ conducted within a month of each other (Liodakis et al. 2022). Further IXPE and VLBA observations of HSP blazars are needed to confirm whether, and if so, why, Mrk 421 is different in this regard.

We have found that the X-ray flux and hardness ratio of Mrk 421 were less variable during Obs. 1 and Obs. 4, when ψ_{X} was essentially constant, than during the ψ_{X} rotation of Obs. 2 and Obs. 3. This implies different physical conditions within the jet between the rotating and nonrotating states. Instead, the similar values of Π_{X} across all observations suggest that the basic particle acceleration scenario remained roughly independent of the magnetic field geometry. This can be accommodated

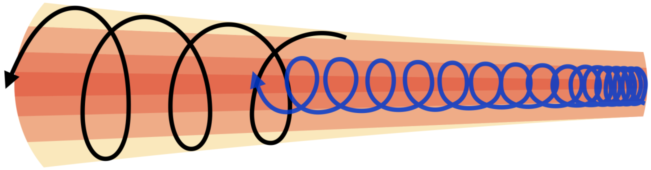

Fig. 8. Schematic diagram of double helical magnetic field components inside the jet. The downstream direction of the jet is to the left. The arrows indicate each helical magnetic field component involved in the emission at different wavelengths (X-ray in blue and longer wavelengths in black).

within the energy-stratified shock scenario, since the degree of order of the magnetic field could be similar whether the shock moves along a straight or helical trajectory. The flux and spectral variations during the rotation event could have been caused by changes in the Doppler factor as the shock executed helical motion, although the data are too sparsely sampled to test this. Future X-ray spectroscopic and polarimetric observations with improved time resolution can potentially test whether spiral motion along a helical magnetic field causes cyclical Doppler factor variations that lead to observed variations in flux, hardness ratio, and polarization. Our examination of a sequence of 43 GHz VLBA images has revealed the presence of a prominent, highly polarized knot moving away from the "core" at a speed of 0.7c during a time span that includes Obs. 1 – Obs. 3 (see Fig. A.3).

This finding suggests a potential connection between the morphological changes near the jet core region and the variability in polarization, as discussed in Di Gesu et al. (2023). The knot could represent a shock containing relativistic electrons accelerated up to Lorentz factor $\sim 10^6$ that radiate at X-ray energies. However, in this scenario, it is difficult to explain the difference in the behavior of ψ_X between Obs. 1 and Obs. 2 – Obs. 3, unless the geometry of the magnetic field varies across the core, with a tighter helical structure toward the downstream end. However, our analysis does not indicate a direct connection between the X-ray polarization position angle and that of either the core or knot P (see Fig. A.5), although the degree of polarization of P, 15–20%, is comparable to Π_X. This apparent lack of connection supports the conclusion, drawn above, that emission regions at longer wavelengths (millimeter, infrared, and optical) were separate from, or only partially coincident with, that of the X-ray emission.

In the case of Obs. 4, there is no apparent connection between the values of ψ of the polarized features in the jet observed on 2022 December 6 (MJD 59919) and ψ_X (Fig. A.5). However, Fig. A.4 indicates an increase in the core flux density in 2023 February (MJD 59986) that could be a signature of an emerging moving feature that would have been upstream of the 43 GHz very-long-baseline interferometry (VLBI) core during IXPE Obs. 4. Further combined IXPE and VLBI monitoring could help in clarifying whether there is any relation between the X-ray emission regions and features seen in the jet at millimeter wavelengths.

We note that, from Obs. 1 to Obs. 3, the polarization angle at optical, infrared, and radio wavelengths rotated in the opposite direction relative to the 5-day rotation of ψ_X during Obs. 2 and Obs. 3. This finding supports the conclusion that the X-ray emission region is separate from that at longer wavelengths. The observed similarity in radio to optical polarization properties implies that the emission at these wavelengths originates from spatially interconnected regions. The longer (relative to X-ray) rotation timescale suggests that the X-ray emission region is smaller than that of these other wavelengths. Although the polarization vector rotation at longer wavelengths could be explained by propagation of a larger emission feature down a helical magnetic field (as in Fig. 8), the long-term behavior of the optical polarization of Mrk 421 implies stochastic, rather than systematic, variations in both ψ_O and Π_O (Marscher & Jorstad 2022).

5. Conclusions

We have reported X-ray, optical, infrared, and radio polarization and flux measurements of the HSP blazar Mrk 421, including four IXPE pointings from between 2022 May and December. Such observations probe the magnetic field structure and particle acceleration mechanisms inside the jets of blazars. The combined 7 months of observations sample the time and energy dependence of the X-ray polarization. Over this time span, ψ_X varied over the full range of ~180°, including a 5-day episode of rotation, while the degree of polarization stayed between ~10 and 15% across all IXPE pointings. The X-ray flux varied by a higher fraction during the rotation than during the two IXPE observations without rotations.

The simultaneous multiwavelength polarimetry results over four IXPE observations provide evidence useful for constraining the physics of the jet. The degree of X-ray polarization was typically ~2–3 times greater than that at longer wavelengths at all epochs sampled, while the polarization angles fluctuated. The discrepancy between the X-ray results compared with radio, infrared, and optical polarimetry supports the previous conclusion that the X-ray emission region is distinct from that at longer wavelengths in HSP blazars (Liodakis et al. 2022; Di Gesu et al. 2022, 2023). As with previous studies, we conclude that the observations are consistent with the energy stratified shock model, with the level of turbulence increasing with distance from the shock front.

One difference between Mrk 421 and Mrk 501 is that there is no apparent correlation between the direction of the jet from VLBA and ψ_X in the former. While this could be due to the bending of the jet from the X-ray to the radio emitting region, amplified by the narrow angle to the line of sight, the optical polarization angle is also much more variable in Mrk 421 than in Mrk 501 (Marscher & Jorstad 2022). This implies an intrinsic difference between the two objects that should be explored with further observations.

Following Di Gesu et al. (2023), we propose a linear stratification scenario and a radial stratification scenario to explain the rotation behavior of ψ_X. The accompanying spectral variation during the ψ_X rotation suggests that the physical conditions of the jet, such as the energy distribution of relativistic electrons, differed between the periods of rotation and non-rotation. In addition, we report rotation in the opposite direction of the ψ between the X-ray and other wavelengths, with the latter occurring over a much longer timescale. This could potentially be interpreted as the presence of multi-helical magnetic field structures inside the jet. Morphological changes in the parsec-scale jet, possibly associated with the contemporaneous emergence of a new knot of emission observed to move down the jet in 43 GHz VLBA images, may be linked to the ψ_X rotation, although differences in the radio and X-ray polarization angles are evidence against such a connection.

In conclusion, the present study continues to develop a new perspective on the physical and geometrical features of the magnetic field inside the jets of blazars by employing polarimetry that extends from radio to X-ray wavelengths. The IXPE observations, which incorporate data at other wavelengths, have played a significant role in constraining the emission arising from the innermost regions of the jet. The polarization properties, sampled over different timescales and energy regimes, suggest a possible connection between spectral and polarization variations. The connection may include morphological changes in radio images, which coincided with a period of ψ_X rotation. However, due to infrequent data sampling, there remain uncertainties regarding apparent correlations, which can be chance coincidences. In addition, IXPE observations of Mrk 421 thus far have been obtained when the blazar was in average activity states. It is of great interest to determine whether the polarization and physical properties change during strong flaring events. As the IXPE mission continues, further studies of Mrk 421 and other blazars are expected to provide the data needed to improve our understanding of the magnetic field geometry and particle acceleration processes in relativistic jets.

Acknowledgements. The authors thank the anonymous referee for comments that improved this manuscript. The Imaging X-ray Polarimetry Explorer (IXPE) is a joint US and Italian mission. The US contribution is supported by the National Aeronautics and Space Administration (NASA) and led and managed by its Marshall Space Flight Center (MSFC), with industry partner Ball Aerospace (contract NNM15AA18C). The Italian contribution is supported by the Italian Space Agency (Agenzia Spaziale Italiana, ASI) through contract ASI-OHBI-2017-12-I.0, agreements ASI-INAF-2017-12-H0 and ASI-INFN-2017.13-H0, and its Space Science Data Center (SSDC), and by the Istituto Nazionale di Astrofisica (INAF) and the Istituto Nazionale di Fisica Nucleare (INFN) in Italy. This research used data products provided by the IXPE Team (MSFC, SSDC, INAF, and INFN) and distributed with additional software tools by the High-Energy Astrophysics Science Archive Research Center (HEASARC), at NASA Goddard Space Flight Center (GSFC). The IAA-CSIC group acknowledges financial support from the grant CEX2021-001131-S funded by MCIN/AEI/10.13039/501100011033 to the Instituto de Astrofísica de Andalucía-CSIC and through grant PID2019-107847RB-C44. The QUIVER data are based on observations with the 100-m Telescope of the MPIfR (Max-Planck-Institut für Radioastronomie) at Effelsberg. Observations with the 100-m radio Telescope at Effelsberg have received funding from the European Union's Horizon 2020 research and innovation programme under grant agreement No 101004719 (ORP). The POLAMI observations were carried out at the IRAM 30m Telescope. IRAM is supported by INSU/CNRS (France), MPG (Germany), and IGN (Spain). Some of the data are based on observations collected at the Observatorio de Sierra Nevada, owned and operated by the Instituto de Astrofísica de Andalucía (IAA-CSIC). Further data are based on observations collected at the Centro Astronómico Hispano en Andalucía (CAHA), operated jointly by Junta de Andalucía and Consejo Superior de Investigaciones Científicas (IAA-CSIC). The Submillimetre Array is a joint project between the Smithsonian Astrophysical Observatory and the Academia Sinica Institute of Astronomy and Astrophysics and is funded by the Smithsonian Institution and the Academia Sinica. Mauna Kea, the location of the SMA, is a culturally important site for the indigenous Hawaiian people; we are privileged to study the cosmos from its summit. Some of the data reported here are based on observations made with the Nordic Optical Telescope, owned in collaboration with the University of Turku and Aarhus University, and operated jointly by Aarhus University, the University of Turku, and the University of Oslo, representing Denmark, Finland, and Norway, the University of Iceland and Stockholm University at the Observatorio del Roque de los Muchachos, La Palma, Spain, of the Instituto de Astrofisica de Canarias. E. L. was supported by Academy of Finland projects 317636 and 320045. The data presented here were obtained [in part] with ALFOSC, which is provided by the Instituto de Astrofisica de Andalucia (IAA) under a joint agreement with the University of Copenhagen and NOT. We acknowledge funding to support our NOT observations from the Finnish Centre for Astronomy with ESO (FINCA), University of Turku, Finland (Academy of Finland grant nr 306531). We are grateful to Vittorio Braga, Matteo Monelli, and Manuel Sänchez Benavente for performing the observations at the Nordic Optical Telescope. Part of the French contributions is supported by the Scientific Research National Center (CNRS) and the French spatial agency (CNES). The research at Boston University was supported in part by National Science Foundation grant AST-2108622, NASA Fermi Guest Investigator grants 80NSSC21K1917 and 80NSSC22K1571, and NASA *Swift* Guest Investigator grant 80NSSC22K0537. This study was based in part on observations conducted using the Perkins Telescope Observatory (PTO) in Arizona, USA, which is owned and operated by Boston University. This research was conducted in part using the Mimir instrument, jointly developed at Boston University and Lowell Observatory and supported by NASA, NSF, and the W.M. Keck Foundation. We thank D. Clemens for guidance in the analysis of the Mimir data. This work was supported by JST, the establishment of university fellowships toward the creation of science and technology innovation, Grant Number JPMJFS2129. This work was supported by Japan Society for the Promotion of Science (JSPS) KAKENHI Grant Numbers JP21H01137. This work was also partially supported by the Optical and Near-Infrared Astronomy Inter-University Cooperation Program from the Ministry of Education, Culture, Sports, Science and Technology (MEXT) of Japan. We are grateful to the observation and operating members of the Kanata Telescope. This research has made use of data from the RoboPol program, a collaboration between Caltech, the University of Crete, IA-FORTH, IUCAA, the MPIfR, and the Nicolaus Copernicus University, which was conducted at Skinakas Observatory in Crete, Greece. D.B., S.K., R.S., N. M., acknowledge support from the European Research Council (ERC) under the European Unions Horizon 2020 research and innovation program under grant agreement No. 771282. C.C. acknowledges support from the European Research Council (ERC) under the HORIZON ERC Grants 2021 program under grant agreement No. 101040021. We acknowledge the use of public data from the *Swift* data archive. Based on observations obtained with *XMM-Newton*, an ESA science mission with instruments and contributions directly funded by ESA Member States and NASA. The Very Long Baseline Array is an instrument of the National Radio Astronomy Observatory. The National Radio Astronomy Observatory is a facility of the National Science Foundation operated under a cooperative agreement by Associated Universities, Inc. S. Kang, S.-S. Lee, W. Y. Cheong, S.-H. Kim, and H.-W. Jeong were supported by the National Research Foundation of Korea (NRF) grant funded by the Korea government (MIST) (2020R1A2C2009003). The KVN is a facility operated by the Korea Astronomy and Space Science Institute. The KVN operations are supported by KREONET (Korea Research Environment Open NETwork) which is managed and operated by KISTI (Korea Institute of Science and Technology Information). The VLBA is an instrument of the National Radio Astronomy Observatory. The National Radio Astronomy Observatory is a facility of the National Science Foundation operated under cooperative agreement by Associated Universities, Inc.

References

Abdo, A. A., Ackermann, M., Agudo, I., et al. 2010, ApJ, 716, 30
Agudo, I., Thum, C., Wiesemeyer, H., et al. 2012, A&A, 541, A111
Aharonian, F. A. 2000, New Astron., 5, 377
Akitaya, H., Moritani, Y., Ui, T., et al. 2014, in Ground-based and Airborne Instrumentation for Astronomy V, eds. S. K. Ramsay, I. S. McLean, & H. Takami, SPIE Conf. Ser., 9147, 914740
Arnaud, K. A. 1996, in Astronomical Data Analysis Software and Systems V, eds. G. H. Jacoby, & J. Barnes, ASP Conf. Ser., 101, 17
Aumont, J., Conversi, L., Thum, C., et al. 2010, A&A, 514, A70
Baldini, L., Barbanera, M., Bellazzini, R., et al. 2021, Astropart. Phys., 133, 102628
Baldini, L., Bucciantini, N., Lalla, N. D., et al. 2022, SoftwareX, 19, 101194
Baloković, M., Paneque, D., Madejski, G., et al. 2016, ApJ, 819, 156
Bellazzini, R., Angelini, F., Baldini, L., et al. 2003, in Polarimetry in Astronomy, ed. S. Fineschi, SPIE Conf. Ser., 4843, 372
Bellazzini, R., Spandre, G., Minuti, M., et al. 2007, Nucl. Instrum. Methods Phys. Res. A, 579, 853
Blinov, D., Pavlidou, V., Papadakis, I., et al. 2015, MNRAS, 453, 1669
Blinov, D., Pavlidou, V., Papadakis, I. E., et al. 2016a, MNRAS, 457, 2252
Blinov, D., Pavlidou, V., Papadakis, I., et al. 2016b, MNRAS, 462, 1775
Blinov, D., Pavlidou, V., Papadakis, I., et al. 2018, MNRAS, 474, 1296
Böttcher, M. 2019, Galaxies, 7, 20
Böttcher, M., Reimer, A., Sweeney, K., & Prakash, A. 2013, ApJ, 768, 54
Chhotray, A., Nappo, F., Ghisellini, G., et al. 2017, MNRAS, 466, 3544
Costa, E., Soffitta, P., Bellazzini, R., et al. 2001, Nature, 411, 662
Dermer, C. D., & Schlickeiser, R. 1993, ApJ, 416, 458
Di Gesu, L., Donnarumma, I., Tavecchio, F., et al. 2022, ApJ, 938, L7
Di Gesu, L., Marshall, H. L., Ehlert, S. R., et al. 2023, Nat. Astron., 7, 1245
Di Marco, A., Costa, E., Muleri, F., et al. 2022, AJ, 163, 170
Di Marco, A., Soffitta, P., Costa, E., et al. 2023, AJ, 165, 143
Donnarumma, I., Vittorini, V., Vercellone, S., et al. 2009, ApJ, 691, L13
Ehlert, S. R., Ferrazzoli, R., Marinucci, A., et al. 2022, ApJ, 935, 116
Fabiani, S., Costa, E., Bellazzini, R., et al. 2012, Adv. Space Res., 49, 143
Fabiani, S., & Muleri, F. 2014, Astronomical X-Ray Polarimetry, Astronomia e astrofisica (Aracne)
Fossati, G., Maraschi, L., Celotti, A., Comastri, A., & Ghisellini, G. 1998, MNRAS, 299, 433
Fraija, N., Benítez, E., Hiriart, D., et al. 2017, ApJS, 232, 7
Gianolli, V. E., Kim, D. E., Bianchi, S., et al. 2023, MNRAS, 523, 4468
HI4PI Collaboration (Ben Bekhti, N., et al.) 2016, A&A, 594, A116

Ho, P. T. P., Moran, J. M., & Lo, K. Y. 2004, ApJ, 616, L1
Hovatta, T., & Lindfors, E. 2019, New Astron. Rev., 87, 101541
Hovatta, T., Lindfors, E., Blinov, D., et al. 2016, A&A, 596, A78
Jermak, H., Steele, I. A., Lindfors, E., et al. 2016, MNRAS, 462, 4267
Jones, T. W., O'Dell, S. L., & Stein, W. A. 1974, ApJ, 188, 353
Jorstad, S. G., Marscher, A. P., Morozova, D. A., amp, , et al. 2017, ApJ, 846, 98
Kang, S., Lee, S.-S., & Byun, D.-Y. 2015, J. Korean Astron. Soc., 48, 257
Kawabata, K. S., Okazaki, A., Akitaya, H., et al. 1999, PASP, 111, 898
Kislat, F., Clark, B., Beilicke, M., & Krawczynski, H. 2015, Astropart. Phys., 68, 45
Kraus, A., Krichbaum, T. P., Wegner, R., et al. 2003, A&A, 401, 161
Lico, R., Giroletti, M., Orienti, M., amp, , et al. 2012, A&A, 545, id A117
Liodakis, I., Peirson, A. L., & Romani, R. W. 2019, ApJ, 880, 29
Liodakis, I., Marscher, A. P., Agudo, I., et al. 2022, Nature, 611, 677
Lister, M. L., Homan, D. C., Kellermann, K. I., amp, , et al. 2021, ApJ, 923, 30
Mannheim, K. 1993, A&A, 269, 67
Maraschi, L., Ghisellini, G., & Celotti, A. 1992, ApJ, 397, L5
Marrone, D. P., & Rao, R. 2008, in Millimeter and Submillimeter Detectors and Instrumentation for Astronomy IV, eds. W. D. Duncan, W. S. Holland, S. Withington, & J. Zmuidzinas, SPIE Conf. Ser., 7020, 70202B
Marscher, A. P., & Gear, W. K. 1985, ApJ, 298, 114
Marscher, A. P., & Jorstad, S. G. 2022, Universe, 8, 644
Marscher, A. P., Jorstad, S. G., D'Arcangelo, F. D., et al. 2008, Nature, 452, 966
Marscher, A. P., Jorstad, S. G., Larionov, V. M., et al. 2010, ApJ, 710, L126
Marshall, H. L. 2021a, ApJ, 907, 82
Marshall, H. L. 2021b, AJ, 162, 134
Massaro, E., Perri, M., Giommi, P., & Nesci, R. 2004, A&A, 413, 489
Middei, R., Giommi, P., Perri, M., et al. 2022, MNRAS, 514, 3179
Middei, R., Perri, M., Puccetti, S., et al. 2023, ApJ, 953, L28
Muleri, F. 2022, in Handbook of X-ray and Gamma-ray Astrophysics, eds. C. Bambi, & A. Santangelo (Springer Living Reference Work), 6
Myserlis, I., Angelakis, E., Kraus, A., et al. 2018, A&A, 609, A68
Nilsson, K., Pasanen, M., Takalo, L. O., et al. 2007, A&A, 475, 199
Piconcelli, E., Jimenez-Bailón, E., Guainazzi, M., et al. 2004, MNRAS, 351, 161
Primiani, R. A., Young, K. H., Young, A., et al. 2016, J. Astron. Instrum., 5, 1641006
Rankin, J., Muleri, F., Tennant, A. F., et al. 2022, AJ, 163, 39
Rybicki, G. B., & Lightman, A. P. 1979, Radiative Processes in Astrophysics (New York: Wiley)
Sikora, M., Begelman, M. C., & Rees, M. J. 1994, ApJ, 421, 153
Strohmayer, T. E. 2017, ApJ, 838, 72
Tavecchio, F. 2021, Galaxies, 9, 37
Tavecchio, F., Landoni, M., Sironi, L., & Coppi, P. 2018, MNRAS, 480, 2872
Weaver, Z. R., Jorstad, S. G., Marscher, A. P., et al. 2022, ApJS, 260, 12
Weisskopf, M. C., Soffitta, P., Baldini, L., et al. 2022, J. Astron. Telesc. Instrum. Syst., 8, 026002
Wilms, J., Allen, A., & McCray, R. 2000, ApJ, 542, 914
Zhang, H. 2019, Galaxies, 7, 85

---

[1] INAF – Istituto di Astrofisica e Planetologia Spaziali, Via del Fosso del Cavaliere 100, 00133 Roma, Italy
e-mail: `dawoon.kim@inaf.it`

[2] Dipartimento di Fisica, Università degli Studi di Roma "La Sapienza", Piazzale Aldo Moro 5, 00185 Roma, Italy

[3] Dipartimento di Fisica, Università degli Studi di Roma "Tor Vergata", Via della Ricerca Scientifica 1, 00133 Roma, Italy

[4] ASI – Agenzia Spaziale Italiana, Via del Politecnico snc, 00133 Roma, Italy

[5] Finnish Centre for Astronomy with ESO, 20014 University of Turku, Finland

[6] Institute for Astrophysical Research, Boston University, 725 Commonwealth Avenue, Boston, MA 02215, USA

[7] Saint Petersburg State University, 7/9 Universitetskaya nab., St. Petersburg 199034, Russia

[8] Space Science Data Center, Agenzia Spaziale Italiana, Via del Politecnico snc, 00133 Roma, Italy

[9] INAF – Osservatorio Astronomico di Roma, Via Frascati 33, 00078 Monte Porzio Catone (RM), Italy

[10] MIT Kavli Institute for Astrophysics and Space Research, Massachusetts Institute of Technology, 77 Massachusetts Avenue, Cambridge, MA 02139, USA

[11] Instituto de Astrofísica de Andalucía-CSIC, Glorieta de la Astronomía s/n, 18008 Granada, Spain

[12] INAF – Osservatorio Astronomico di Brera, Via E. Bianchi 46, 23807 Merate (LC), Italy

[13] Dipartimento di Fisica, Universitá degli Studi di Torino, Via Pietro Giuria 1, 10125 Torino, Italy

[14] Istituto Nazionale di Fisica Nucleare, Sezione di Torino, Via Pietro Giuria 1, 10125 Torino, Italy

[15] University of Maryland, Baltimore County, Baltimore, MD 21250, USA

[16] NASA Goddard Space Flight Center, Greenbelt, MD 20771, USA

[17] Louisiana State University, Baton Rouge, LA 70803, USA

[18] Istituto Nazionale di Fisica Nucleare, Sezione di Roma "Tor Vergata", Via della Ricerca Scientifica 1, 00133 Roma, Italy

[19] Department of Astronomy, University of Maryland, College Park, Maryland 20742, USA

[20] Hiroshima Astrophysical Science Center, Hiroshima University, 1-3-1 Kagamiyama, Higashi-Hiroshima, Hiroshima 739-8526, Japan

[21] Department of Physics, Graduate School of Advanced Science and Engineering, Hiroshima University Kagamiyama, 1-3-1 Higashi-Hiroshima, Hiroshima 739-8526, Japan

[22] Core Research for Energetic Universe (Core-U), Hiroshima University, 1-3-1 Kagamiyama, Higashi-Hiroshima, Hiroshima 739-8526, Japan

[23] Department of Physics, Tokyo Institute of Technology, 2-12-1 Ookayama, Meguro-ku, Tokyo 152-8551, Japan

[24] Planetary Exploration Research Center, Chiba Institute of Technology, 2-17-1 Tsudanuma, Narashino, Chiba 275-0016, Japan

[25] Institut de Radioastronomie Millimétrique, Avenida Divina Pastora 7, Local 20, 18012 Granada, Spain

[26] Max-Planck-Institut für Radioastronomie, Auf dem Hügel 69, 53121 Bonn, Germany

[27] Section of Astrophysics, Astronomy & Mechanics, Department of Physics, National and Kapodistrian University of Athens, Panepistimiopolis, Zografos 15784, Greece

[28] Korea Astronomy and Space Science Institute, Daedeokdae-ro 776, Yuseong-gu, Daejeon 34055, Republic of Korea

[29] University of Science and Technology, Gajeong-ro 217, Yuseong-gu, Daejeon 34113, Republic of Korea

[30] Center for Astrophysics | Harvard & Smithsonian, 60 Garden St, Cambridge, MA 02138, USA

[31] Department of Physics and Astronomy, 20014 University of Turku, Finland

[32] Department of Physics, University of Crete, 70013 Heraklion, Greece

[33] Institute of Astrophysics, Foundation for Research and Technology-Hellas, 71110 Heraklion, Greece

[34] Owens Valley Radio Observatory, California Institute of Technology, MC 249-17, Pasadena, CA 91125, USA

[35] Special Astrophysical Observatory, Russian Academy of Sciences, 369167 Nizhnii Arkhyz, Russia

[36] Pulkovo Observatory, St.Petersburg 196140, Russia

[37] INAF – Osservatorio Astronomico di Cagliari, Via della Scienza 5, 09047 Selargius (CA), Italy

[38] Istituto Nazionale di Fisica Nucleare, Sezione di Pisa, Largo B. Pontecorvo 3, 56127 Pisa, Italy

[39] Dipartimento di Fisica, Universitá di Pisa, Largo B. Pontecorvo 3, 56127 Pisa, Italy

[40] NASA Marshall Space Flight Center, Huntsville, AL 35812, USA

[41] Dipartimento di Matematica e Fisica, Università degli Studi Roma Tre, Via della Vasca Navale 84, 00146 Roma, Italy

[42] INAF – Osservatorio Astrofisico di Arcetri, Largo Enrico Fermi 5, 50125 Firenze, Italy

[43] Dipartimento di Fisica e Astronomia, Universitá degli Studi di Firenze, Via Sansone 1, 50019 Sesto Fiorentino (FI), Italy

[44] Istituto Nazionale di Fisica Nucleare, Sezione di Firenze, Via Sansone 1, 50019 Sesto Fiorentino (FI), Italy

[45] Science and Technology Institute, Universities Space Research Association, Huntsville, AL 35805, USA

[46] Department of Physics and Kavli Institute for Particle Astrophysics and Cosmology, Stanford University, Stanford, California 94305, USA
[47] Institut für Astronomie und Astrophysik, Universität Tübingen, Sand 1, 72076 Tübingen, Germany
[48] Astronomical Institute of the Czech Academy of Sciences, Boční II 1401/1, 14100 Praha 4, Czech Republic
[49] RIKEN Cluster for Pioneering Research, 2-1 Hirosawa, Wako Saitama 351-0198, Japan
[50] California Institute of Technology, Pasadena, CA 91125, USA
[51] Yamagata University, 1-4-12 Kojirakawa-machi Yamagata-shi 990-8560, Japan
[52] Osaka University, 1-1 Yamadaoka, Suita, Osaka 565-0871, Japan
[53] University of British Columbia, Vancouver, BC V6T 1Z4, Canada
[54] Department of Physics, Faculty of Science and Engineering, Chuo University, 1-13-27 Kasuga, Bunkyo-ku, Tokyo 112-8551, Japan
[55] Department of Physics and Astronomy and Space Science Center, University of New Hampshire, Durham, NH 03824, USA
[56] Physics Department and McDonnell Center for the Space Sciences, Washington University in St. Louis, St. Louis, MO 63130, USA
[57] Université de Strasbourg, CNRS, Observatoire Astronomique de Strasbourg, UMR 7550, 67000 Strasbourg, France
[58] Graduate School of Science, Division of Particle and Astrophysical Science, Nagoya University, Furo-cho, Chikusa-ku, Nagoya, Aichi 464-8602, Japan
[59] Department of Physics, The University of Hong Kong, Pokfulam, Hong Kong
[60] Department of Astronomy and Astrophysics, Pennsylvania State University, University Park, PA 16802, USA
[61] Université Grenoble Alpes, CNRS, IPAG, 38000 Grenoble, France
[62] Dipartimento di Fisica e Astronomia, Universitá degli Studi di Padova, Via Marzolo 8, 35131 Padova, Italy
[63] Mullard Space Science Laboratory, University College London, Holmbury St Mary, Dorking, Surrey RH5 6NT, UK
[64] Anton Pannekoek Institute for Astronomy & GRAPPA, University of Amsterdam, Science Park 904, 1098 XH Amsterdam, The Netherlands
[65] Guangxi Key Laboratory for Relativistic Astrophysics, School of Physical Science and Technology, Guangxi University, Nanning 530004, PR China

Appendix A: Observation and data reduction

A.1. IXPE data

We obtained cleaned level 2 IXPE data processed by a standard IXPE pipeline from the Science Operation Center (SOC)[2]. The pipeline includes the photoelectron events correction in the GPD (Costa et al. 2001; Bellazzini et al. 2007; Fabiani et al. 2012; Baldini et al. 2021), as well as the photo-electron track reconstruction process based on standard moments analysis (Bellazzini et al. 2003; Fabiani & Muleri 2014; Di Marco et al. 2022). In particular, the pipeline rectifies the fluctuations in gain properties affected by gas conditions (e.g., temperature and pressure), nonuniform charging of the gas electron multiplier material, and polarization artifacts induced by spurious modulation (Rankin et al. 2022). The level 2 data of IXPE contain the time of arrival, position, and energy of each photon event, along with polarization information represented by the Q and U Stokes parameters.

The scientific data analysis was performed using the public `ixpeobssim` software version 30.2.1 (Baldini et al. 2022). First, we extracted the source and background data using an optimized region selection criterion as suggested by Di Marco et al. (2023). The source data were extracted from a circular region with a 60″radius, while the background data were extracted from an annular source-free region with inner and outer radii of 150″and 300″, respectively. Both regions were centered on the source position in the detector frame. Next, we created the polarization cube (`PCUBE`) and the Stokes parameter spectra (I, Q, and U) using `xpbin`. To eliminate the influence due to the background, we applied the background subtraction technique (Baldini et al. 2022) and created `PCUBE`s of the source and background for each DU. The final source polarization properties were recalibrated by considering the `BACKSCALE` ratio between the source and background ($\sim$ 0.05). In a similar way, we produced three Stokes parameter spectra for three detectors, totaling 9 spectra, using the `PHA1`, `PHAQ`, and `PHAU` algorithms in `xpbin`. We grouped the Ispectra with a minimum of 30 counts in each energy bin, as required for the χ^2 statistics in the fits, and applied constant energy binning for the $Q$and Uspectra for every 0.2 keV interval. We employed the recent version of the IXPE calibration database files (CALDB 20221020) contained in both `ixpeobssim` and the HEASOFT package (v6.31.1) for both the `PCUBE` and the Stokes parameter spectra. In particular, we utilized the weighted analysis method (Di Marco et al. 2022) on the I, Q, and Uspectra to improve the significance of our measurements with `alpha075` response matrices. The flux variability was analyzed using a light curve created with the `LC` algorithms in `xpbin` of `ixpeobssim`.

The polarization error contour (Fig. 1) was drawn from calibrated normalized $\mathcal{Q}(= Q/I)$ and $\mathcal{U}(= U/I)$ at specific confidence levels (68.27%, 90.00%, and 99.00%) according to

$$\begin{aligned} \mathcal{Q}_{C.L.} &= \mathcal{Q}_0 + \epsilon\cos(\zeta), \\ \mathcal{U}_{C.L.} &= \mathcal{U}_0 + \epsilon\sin(\zeta), \end{aligned} \tag{A.1}$$

where $\mathcal{Q}_0$ and $\mathcal{U}_0$ represent the averaged Stokes parameter values, and $\mathcal{Q}_{C.L.}$ and $\mathcal{U}_{C.L.}$ denote the $\mathcal{Q}$ and $\mathcal{U}$ values of a given confidence level calculated with two degrees of freedom, respectively. We note that, since we are considering two dependent variables, Π and ψ, at the same time, the error should be recalculated based on the χ^2 distribution with 2 degrees of freedom ($\epsilon = \sigma\sqrt{\chi^2_{2\,\mathrm{d.o.f.}}}$, $\sigma = \sigma_{\mathcal{Q}} = \sigma_{\mathcal{U}}$). The variable ζ follows the angle distribution from 0 to 2π.

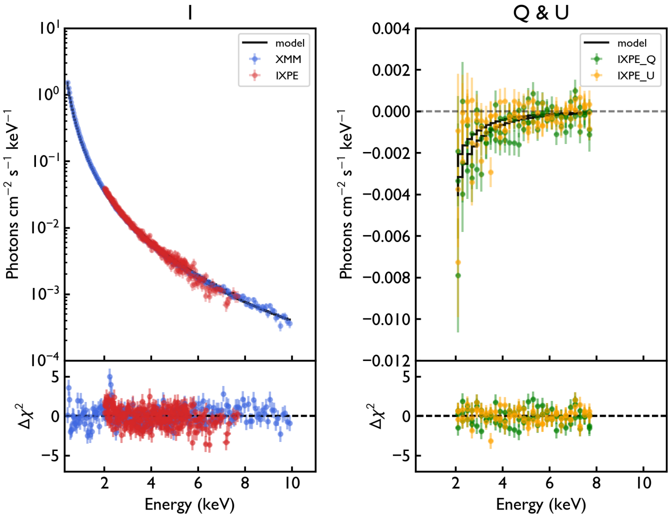

Fig. A.1. Spectropolarimetric fit of *XMM-Newton* (blue) and IXPE I (red), Q (green), and U (orange) spectra, with residuals of the best-fit model. The left panel displays the I spectrum with a log-parabolic model (Massaro et al. 2004), while the right panel presents the constant polarization model fit with the `POLCONST` model for Q and U spectra. The black line in both panels indicates the model fit result.

Table A.1. Best-fit parameters from our simultaneous spectropolarimetric analysis.

MODEL = CONSTANT × TBABS × LOGPAR × POLCONST			
Component	Parameter	Units	Value (±1σ)
LOGPAR	α		2.82 ±0.005
	β		0.20 ±0.004
	pivot E	keV	5. (f)
	Norm		2.96e-3 ±1.e-5
POLCONST	Π_X	(%)	14 ±1
	ψ_X	(°)	107 ±3
TBABS	N_H	10^{22}cm^{-2}	1.34e-2 (f)
CONSTANT	*XMM-Newton*		1. (f)
	IXPE DU 1		1.11 ± 0.005
	IXPE DU 2		1.06 ± 0.005
	IXPE DU 3		1.01 ± 0.005
			χ^2 / d.o.f.= 740/650

Notes. Errors are 1σ confidence and (f) denotes a fixed parameter.

A.2. Spectroscopic X-ray data

During IXPE Obs. 4, a snapshot of about 5 ks was performed with *XMM-Newton* in timing mode to limit photon pile-up. To extract the science products, we used the *XMM-Newton* Science Analysis Software (SAS), version 21, with the most updated current calibration files. Two boxed regions were adopted to extract the source spectra and background. In particular, we chose the source box to have a width of 27 pixels, as this size was found to maximize the signal-to-noise ratio. (Details of this procedure can be found in Piconcelli et al. 2004.) Then, the resulting spectrum was binned to achieve at least 30 counts in each energy bin. To allow simultaneous spectropolarimetric fitting within `XSPEC`, the keyword "XFLT0001 Stokes:0" was added to the headers of the corresponding `PHA` files.

The *Swift*-XRT monitoring consisted of ~1 ks long observations performed in windowed timing (WT) mode. Raw data

---

[2] `https://heasarc.gsfc.nasa.gov/docs/ixpe/analysis/IXPE-SOC-DOC-009-UserGuide-Software.pdf`

Table A.2. Multiwavelength polarization properties of Mrk 421.

Telescope	Band	Dates	Radio Polarization		Radio Flux Density
	(GHz)	(YYYY-MM-DD)	Π_{R}(%)	ψ_{R} (°)	(10^{-25} erg s^{-1} cm^{-2} Hz^{-1})
KVN	22	2022-12-09	2.4 ± 0.7	210 ± 12	45 ± 4
KVN	43	2022-12-09	2.7 ± 0.5	142 ± 9	40 ± 2
KVN	86	2022-12-09	3.1 ± 2.3	153 ± 15	34 ± 7
KVN	129	2022-12-09	4.4 ± 2.0	191 ± 16	71 ± 19
SMA	230	2022-12-07	2.0 ± 0.3	163 ± 3	20 ± 2
Effelsberg	4.85	2022-12-02	0.9 ± 0.2	96 ± 4	59.4 ± 1.0
Effelsberg	8.35	2022-12-02	1.2 ± 0.4	135 ± 5	50.1 ± 0.5
Effelsberg	10.45	2022-12-02	1.2 ± 0.2	159 ± 7	48.7 ± 1.1
VLBA	43	2022-12-06	1.7 ± 0.6	171 ± 10	25.9 ± 3.3
VLBA	43	2022-11-20	2.1 ± 0.4	178 ± 7	22.9 ± 3.3
VLBA	43	2022-11-01	1.5 ± 0.3	181 ± 8	27.5 ± 3.5
VLBA	43	2022-08-21	2.0 ± 0.6	166 ± 9	29.4 ± 3.6
VLBA	43	2022-07-22	1.3 ± 0.5	215 ± 13	28.8 ± 3.6
VLBA	43	2022-07-15	< 1.1	Undetermined	29.0 ± 4.1
Telescope	Band	Dates	Infrared Polarization		Infrared flux density
	(μm)	(YYYY-MM-DD)	Π_{IR}(%)	ψ_{IR} (°)	(10^{-25} erg s^{-1} cm^{-2} Hz^{-1})
Kanata [1]	J:1.1	2022-12-07	2.1 ± 0.03	167.0 ± 0.3	1.65 ± 0.03
Telescope	Band	Dates	Optical Polarization		Optical flux density
	(nm)	(YYYY-MM-DD)	Π_{O}(%)	ψ_{O} (°)	(10^{-25} erg s^{-1} cm^{-2} Hz^{-1})
SNO	R:653	2022-12-07	4.6 ± 1.3	206 ± 9	2.11 ± 0.03
Kanata[1]	R:653	2022-12-07	2.41 ± 0.02	176 ± 0.2	–
Perkins	R:653	2022-12-17	2.65 ± 0.21	151.9 ± 2.0	2.75 ± 0.03
Perkins	R:653	2022-12-17	2.68 ± 0.21	156.2 ± 2.3	2.74 ± 0.03
Perkins	R:653	2022-12-17	2.51 ± 0.21	155.9 ± 2.5	2.75 ± 0.03
Perkins	R:653	2022-12-16	1.12 ± 0.27	156.2 ± 7.2	2.87 ± 0.03
Perkins	R:653	2022-12-15	1.48 ± 0.28	160.6 ± 5.7	2.77 ± 0.03
Perkins	R:653	2022-12-14	1.74 ± 0.30	125.1 ± 5.3	2.72 ± 0.02
Perkins	R:653	2022-12-01	6.89 ± 0.39	161.7 ± 1.8	2.98 ± 0.04
Perkins	R:653	2022-12-01	7.11 ± 0.37	164.5 ± 1.7	2.99 ± 0.03
Perkins	R:653	2022-12-01	6.91 ± 0.37	159.0 ± 1.6	3.00 ± 0.03
Perkins	R:653	2022-11-28	4.76 ± 0.25	179.1 ± 1.6	2.99 ± 0.03
Perkins	R:653	2022-11-28	4.39 ± 0.28	164.4 ± 1.9	3.00 ± 0.04
Perkins	R:653	2022-11-28	5.22 ± 0.22	164.7 ± 1.3	3.00 ± 0.03
Perkins	R:653	2022-11-28	4.22 ± 0.22	168.6 ± 1.6	2.99 ± 0.03
Perkins	R:653	2022-11-27	5.79 ± 0.26	162.3 ± 1.3	2.98 ± 0.03
Perkins	R:653	2022-11-27	5.79 ± 0.21	165.3 ± 0.8	2.99 ± 0.02
Perkins	R:653	2022-11-27	5.02 ± 0.21	163.7 ± 0.8	2.98 ± 0.02
Perkins	R:653	2022-11-27	5.29 ± 0.21	163.3 ± 0.4	2.99 ± 0.02
Perkins	R:653	2022-11-26	6.42 ± 0.21	151.5 ± 0.8	2.86 ± 0.02
Perkins	R:653	2022-11-26	5.71 ± 0.23	152.0 ± 1.1	2.87 ± 0.02
Perkins	R:653	2022-11-26	5.44 ± 0.21	155.0 ± 0.9	2.86 ± 0.02

Notes.[1]Not corrected for dilution of polarization by unpolarized starlight from the host galaxy.

were reduced using the standard commands within the *XRT* Data Analysis Software (XRTDAS, version 3.6.1) and adopting the latest calibration files available in the *Swift*-XRT CALDB (version 20210915). The cleaned event files were used to extract the source spectrum from a circular region with a radius of 47″, while the background was extracted using a blank sky WT observation available in the Swift archive, also within a circular region of radius 47″. The resulting spectra were subsequently binned, requiring at least 25 counts in each energy bin.

A.3. Radio, infrared, and optical data

During all of the IXPE pointings, we observed Mrk 421 at millimeter (radio), infrared, and optical wavelengths, measuring both flux density and linear polarization. The observations and data analysis for the first three observations can be found in detail in Di Gesu et al. (2022, 2023); here we provide only a short description. For Obs. 4, radio, infrared, and optical observations were provided by QUIVER at the Effelsberg telescope, KVN, SMA (Ho et al. 2004), Hiroshima Optical and Near-InfraRed camera (HONIR; Akitaya et al. 2014) at the Kanata Telescope, the Perkins Telescope, and T90 at the SNO.

The QUIVER observations were performed at several radio bands (depending on receiver availability and weather conditions) from 2.6 GHz to 44 GHz (11 cm to 7 mm wavelength) using six receivers located at the secondary focus of the 100-m Effelsberg Radio Telescope (S110mm, S45mm, S28mm,

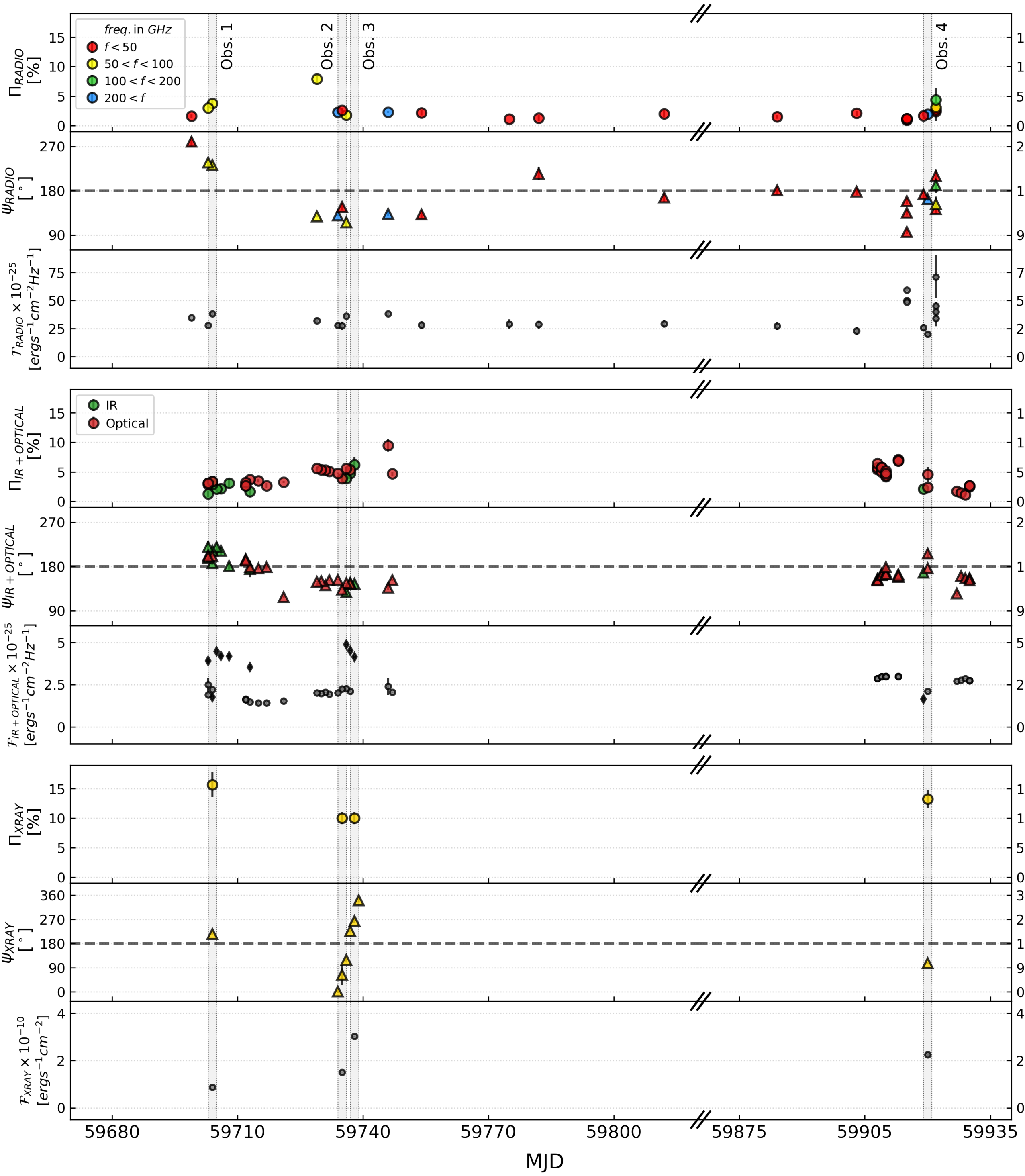

Fig. A.2. Multiwavelength polarization versus time of Mrk 421. Each row presents the polarization degree (circle) and polarization angle (triangle), with 1σ errors measured by radio ($f < 50$ GHz in red, $50 < f < 100$ GHz in yellow, $100 < f < 200$ GHz in green, and $f < 200$ GHz in blue), infrared (green), optical (red), and X-ray (orange) facilities, from top to bottom. The gray shaded areas denote the durations of the four IXPE observations.

S20mm, S14mm, and S7mm). The receivers are equipped with two orthogonally polarized feeds (either circular or linear) that can deliver polarimetric parameters either using conventional polarimeters or by connecting the SpecPol spectropolarimetric backend. Instrumental polarization is calibrated via observations of both polarized and unpolarized calibrators performed in each session, and then removed from the data (e.g., Myserlis et al. 2018; Kraus et al. 2003). The polarized intensity, degree, and position angle were derived from the Stokes I, Q, and U cross-scans. The total flux density was successfully recovered at 13 bands between 4.85 GHz and 43.75 GHz. The calibrators 3C 286, 3C 48, and NGC 7027 were used for the total flux and polarization calibration (e.g., Myserlis et al. 2018; Kraus et al. 2003).

Observations were conducted with the KVN simultaneously at 4 frequencies from 22 to 129 GHz in single-dish mode. This was achieved by using the Tamna (22, 43 GHz) and Yonsei (86,129 GHz) antennas with circularly polarized feed horns to conduct two-frequency dual-polarization observations. The polarization angle was calibrated using the Crab nebula (152°; Aumont et al. 2010), and the polarization degree using Jupiter (unpolarized) and 3C286 (polarized, Agudo et al. 2012) following Kang et al. (2015).

The SMA observations were taken at 225.538 GHz (1.3 mm) through the SMAPOL (SMA Monitoring of AGN with POLarization) program. The SMAPOL observations were taken on 2022 December 7 (MJD 59920) in full polarization mode (Marrone & Rao 2008) using the SWARM correlator (Primiani et al. 2016), and calibrated with the MIR software package[3].

Observations using HONIR were taken on 2022 December 6 (MJD 59919.7537) in the R and J bands[4]. Each observation comprised four exposures in different positions of the half-wave plate (Kawabata et al. 1999), which were then used to estimate the Stokes parameters and calculate the polarization degree and angle. The host galaxy of Mrk 421 contributes a significant fraction of unpolarized flux to the total emission, thereby reducing the polarization. None of the polarization degree estimates from Kanata have been corrected for the host-galaxy contribution due to the lack of the photometry data needed for such a correction, and hence they should be considered as lower limits to the intrinsic polarization degree of the blazar component.

The optical photometric and polarimetric observations were also obtained at the 1.8 m Perkins Telescope (Flagstaff, AZ, USA) with the PRISM camera[5] in the R band performed before and after Obs. 4. The camera includes a polarimeter with a rotating half-wave plate. Each polarization observation has consisted of four consecutive exposures of 60 s at instrumental position angles 0°, 90°, 45°, and 135° of the wave plate to calculate the normalized Stokes parameters Q and U.

The SNO observations were performed using polarized filters oriented to represent different positions of a half-wave plate, similar to a conventional polarimeter. The data are then analyzed following standard photometric procedures. Mrk 421 was observed on 2022 December 7 in the R band. In this case, following Nilsson et al. (2007) and Hovatta et al. (2016), we corrected the host-galaxy contribution. Several observations were taken within the same night. We report the weighted average and uncertainty after considering all of the intra-night observations to account for variations in the system and the observing conditions during the rotation of the filter wheel.

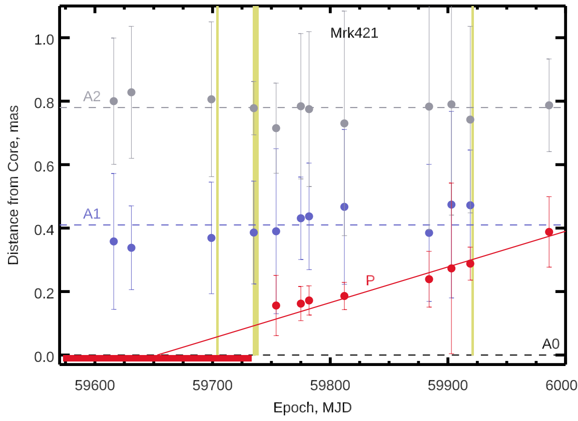

Fig. A.3. Distance from the core of jet components $A1$ (blue circles), $A2$ (gray circles), and P (red circles) versus time. The black dotted line indicates the position of the core, $A0$, the red line approximates the motion of knot P with the uncertainty of its ejection time shown by the red area at the bottom left, and yellow areas mark epochs of IXPE observations.

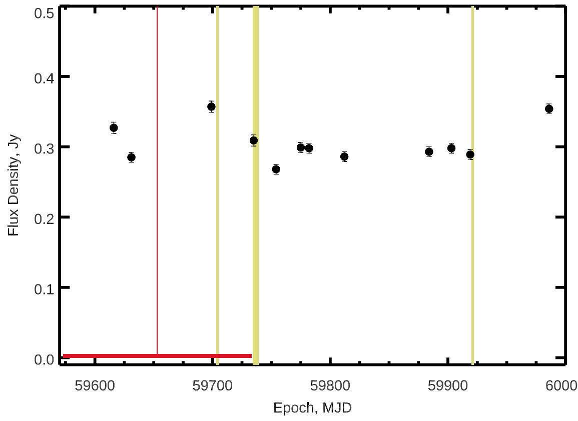

Fig. A.4. Light curve of the core, $A0$. The red vertical line marks the time of the ejection of knot P, with its 1σ uncertainty indicated by the red horizontal line. The yellow areas mark epochs of IXPE observations.

A.4. VLBA observations and analysis

The VLBA data were reduced with the Astronomical Image Process System (AIPS) and *Difmap* software packages in the manner described by Jorstad et al. (2017). The total intensity images are modeled by a number of components with circular Gaussian brightness distributions, with the minimum number of components determined by the best fit between the data and model at each epoch according to a χ^2 test. We identify the brightest feature located at the southeastern end of the jet as the "core," designated as $A0$, which we assume to be a stationary feature. To obtain polarized intensity images, the data were corrected for the instrumental-polarization "D-terms," calculated by averaging the D-terms obtained individually from a number of sources (usually 15) observed along with Mrk 421 in the BEAM-ME program. The electric-vector position angle ($\psi_{43\mathrm{GHz}}$) calibration was obtained by different methods, as discussed in Jorstad et al. (2017). The modeling of total intensity images provides the following parameters of each component: flux density, S, distance from the core, R, position angle with respect to the core, Θ, and angular size of the component, a (full width at half maximum of the best-fit Gaussian). For polarized features in the jet, we calculated the degree of polarization, Π_{knot}, and ψ_{knot} by integrating the Q and U Stokes parameter models obtained with *Difmap* during imaging within the size of the corresponding feature from the total flux density modeling. As a result of modeling, we have detected three stationary features, $A0$, $A1$, and $A2$, and one moving knot, P in the jet of Mrk 421 during 12 epochs from 2022 February 5 to 2023 February 11. Table A.3 gives the average (over epochs) parameters of the jet features, while Fig. A.3 plots the distance of all knots detected in the jet versus time, and Fig. A.4 presents the light curve of the core, $A0$.

We approximated the motion of knot P with a ballistic trajectory with proper motion μ=0.34±0.06 mas yr^{-1}, corresponding

---

[3] https://lweb.cfa.harvard.edu/~cqi/mircook.html

[4] http://hasc.hiroshima-u.ac.jp/instruments/honir/filters-e.html

[5] https://www.bu.edu/prism/

Table A.3. Average parameters of the main features in the jet of Mrk 421 at 43 GHz.

Parameter	A0	A1	A2	P
Number of epochs	12	11	12	8
Average flux, S, (Jy)	0.31 ± 0.03	0.023 ± 0.014	0.017 ± 0.008	0.014 ± 0.010
Average distance, R (mas)	–	0.41 ± 0.05	0.78 ± 0.03	0.23 ± 0.08
Average PA, Θ, (°)	–	−31 ± 10	−45 ± 5	−10 ± 12
Average Size, a, (mas)	0.06 ± 0.02	0.24 ± 0.07	0.46 ± 0.12	0.14 ± 0.07

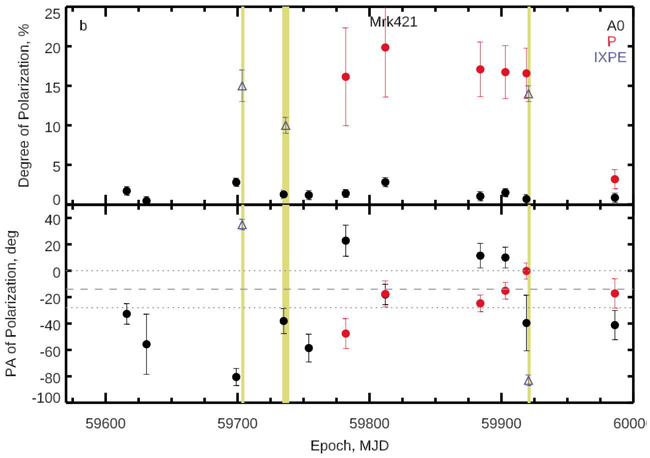

Fig. A.5. Polarization parameters of component $A0$ (black circles) and P (red circles): the degree of polarization (top panel) and the position angle of polarization (bottom panel). The yellow areas mark IXPE observations, while blue triangles plot Π_X and ψ_X; the dashed gray line in the bottom panel shows the direction of the jet according to Weaver et al. (2022), with dotted gray lines indicating its 1σ uncertainty.

to a sub-luminal apparent speed (in units of c) $\beta_{app} = 0.7 \pm 0.1$. The MOJAVE survey [6] at 15 GHz finds an historical maximum $\beta_{app} \sim 0.2$ in the Mrk 421 jet. At 43 GHz, with 3 times higher angular resolution, Weaver et al. (2022) reported three knots with $\beta_{app} > 1$, with the fastest having an apparent speed of 2.41 ± 0.14 c, based on monitoring within the VLBA-BU-BLAZAR program. We extrapolated the motion of P back to the core (as shown in Fig. A.3 by a solid red line), which yields the time of ejection of P from the core [7] as MJD 59653±80 (2022 March 14). Figure A.4 plots the light curve of the core ($A0$), which has a local maximum on MJD 59699 (2022 April 30), the epoch of VLBA observation closest to the ejection time of P; this supports the derived time of ejection. Knot P possesses the highest degree of polarization in the jet, with Π_P reaching ∼20%. Another polarized feature in the jet is the core $A0$, with an average $\Pi_{A0} \sim 2\%$. Figure A.5 shows the evolution of the polarization parameters $\Pi_{\rm A0}$, $\psi_{\rm A0}$ and $\Pi_{\rm P}$, $\psi_{\rm P}$. Figures A.3 and A.5 also indicate the times of the four IXPE observations by yellow areas, with the widest area covering two pointings (Obs. 2 and Obs. 3). Figure A.5 plots the values of $\Pi_{\rm X}$ and ψ_X, except during observations Obs. 2 & Obs. 3, when $\psi_{\rm X}$ rotated at a fast rate of ∼85 °/day (Di Gesu et al. 2023).

Appendix B: Maximum likelihood method of the multicomponent model

The multicomponent model (Pacciani et al., in preparation) comprises (1) a constant component with a steady polarization degree and angle and (2) a rotating component with a constant polarization degree and a rotating polarization angle. The likelihood estimator for this model is

$$S(\Pi_1, \Psi_1, \Pi_2, \Psi_2^0, R_1, \omega) =$$
$$-2\sum_i \ln\Big[1 + \mu_i R_1 \Pi_1 \left(\cos 2\Psi_1 \cos 2\psi_i + \sin 2\Psi_1 \sin 2\psi_i\right) +$$
$$\mu_i (1 - R_1)\Pi_2 \left(\cos 2\Psi_2^0 \cos 2(\psi_i - \omega t) + \sin 2\Psi_2^0 \sin 2(\psi_i - \omega t)\right)\Big], \tag{B.1}$$

where Π_1 and Ψ_1 are the polarization degree and angle of the constant component; Π_2 is the polarization degree of the rotating component, Ψ_2^0 is the initial polarization angle of the rotating component; ω is the rotation rate of the rotating component; R_1 is the relative intensity of the constant component; and μ_i is modulation factor of each event. We note that the fit with this model allows only extraction of the products of $R_1\Pi_1$ and of $(1 - R_1)\Pi_2$. The constant polarization model can be obtained from Eq. B.1 by setting the ratio parameter to $R_1 = 1$. Similarly, the rotation model with constant polarization degree can be obtained by setting $R_1 = 0$.

---

[6] `www.cv.nrao.edu/MOJAVE/sourcepages/1101+384.shtml`

[7] The time of passage of the centroid of P through the centroid of $A0$